
Research Article: New Research | Neuronal Excitability

Deciphering the Contribution of Oriens-Lacunosum/Moleculare (OLM) Cells to Intrinsic Theta Rhythms Using Biophysical Local Field Potential (LFP) Models

Alexandra P. Chatzikalymniou^{1,2} and Frances K. Skinner^{1,3}

¹*Krembil Research Institute, University Health Network, Toronto ON M5T 2S8, Canada*

²*Department of Physiology, University of Toronto, Toronto ON M5T 2S8, Canada*

³*Departments of Medicine (Neurology) and Physiology, University of Toronto, Toronto ON M5S 1A8, Canada*

DOI: 10.1523/ENEURO.0146-18.2018

Received: 11 April 2018

Revised: 3 July 2018

Accepted: 10 July 2018

Published: 22 August 2018

Author contributions: A.C. and F.S. designed research; A.C. performed research; A.C. analyzed data; A.C. and F.S. wrote the paper.

Funding: <http://doi.org/10.13039/501100000038>Gouvernement du Canada | Natural Sciences and Engineering Research Council of Canada (NSERC)
RGPIN 203700-11
RGPIN-2016-06182

Funding: Magaret J Santalo Scholarship (Dept Physiology, University of Toronto)

Funding: Ontario Graduate Scholarship

Funding: Unilever/Lipton OSOTF Graduate Scholarship

Conflict of Interest: Authors report no conflict of interest.

This work was supported by the Natural Sciences and Engineering Research Council of Canada (NSERC) Discovery Grants to FKS. APC was supported by Unilever/Lipton OSOTF Graduate Fellowship, Margaret J. Santalo Scholarship (Dept Physiology, Toronto) and Ontario Graduate Scholarship (OGS).

Correspondence should be addressed to Frances K. Skinner, frances.skinner@gmail.com

Cite as: eNeuro 2018; 10.1523/ENEURO.0146-18.2018

Alerts: Sign up at eneuro.org/alerts to receive customized email alerts when the fully formatted version of this article is published.

Accepted manuscripts are peer-reviewed but have not been through the copyediting, formatting, or proofreading process.

Copyright © 2018 Chatzikalymniou and Skinner

This is an open-access article distributed under the terms of the Creative Commons Attribution 4.0 International license, which permits unrestricted use, distribution and reproduction in any medium provided that the original work is properly attributed.

Manuscript Title:

Deciphering the contribution of oriens-lacunosum/moleculare (OLM) cells to intrinsic theta rhythms using biophysical local field potential (LFP) models

Abbreviated Title:

Cellular contributions to hippocampal theta LFPs

List all Author Names and Affiliations in order as they would appear in the published article:

Alexandra P. Chatzikalymniou^{1,2}, Frances K. Skinner^{1,3}

¹Krembil Research Institute, University Health Network, Toronto, ON, Canada M5T 2S8

²Department of Physiology, University of Toronto, Toronto, ON, Canada M5T 2S8

³Departments of Medicine (Neurology) and Physiology, University of Toronto, Toronto, ON, Canada M5S 1A8

Author Contributions:

All authors designed research; APC performed research and analyzed data; All authors wrote paper

Correspondence should be addressed to (include email address):

FKS (frances.skinner@gmail.com)

Number of Figures: 12

Number of Tables: 1

Number of Multimedia: 0;

Number of words for Abstract: 250

Number of words for Significance Statement: 119

Number of words for Introduction: 748

Number of words for Discussion: 2906

Acknowledgements:

We thank Katie Ferguson for her feedback and participation at early stages of this work, Benedicte Amilhon and Sylvain Williams for their helpful comments, and Alexandre Guet-McCreight for a careful reading of this work. We thank NSERC Canada, Margaret J. Santalo Scholarship (Dept Physiology, Toronto), OGS and the SciNet HPC Consortium for support.

Conflicts of Interest: Authors report no conflict of interest.

Funding Sources: This work was supported by the Natural Sciences and Engineering Research Council of Canada (NSERC) Discovery Grants to FKS. APC was supported by Unilever/Lipton OSOTF Graduate Fellowship, Margaret J. Santalo Scholarship (Dept Physiology, Toronto) and Ontario Graduate Scholarship (OGS).

1 Deciphering the contribution of 2 oriens-lacunosum/moleculare (OLM) 3 cells to *intrinsic* theta rhythms using 4 biophysical local field potential (LFP) 5 models

6 Author Names

8 **Abstract** Oscillations in local field potentials (LFPs) are prevalent and contribute to brain
9 function. An understanding of the cellular correlates and pathways affecting LFPs is needed but
10 many overlapping pathways *in vivo* make this difficult to achieve. A prevalent LFP rhythm in the
11 hippocampus associated with memory processing and spatial navigation is the theta (3-12 Hz)
12 oscillation. Theta rhythms emerge *intrinsically* in an *in vitro* whole hippocampus preparation and
13 this reduced preparation makes it possible to assess the contribution of different cell types to LFP
14 generation. We focus on oriens-lacunosum/moleculare (OLM) cells as a major class of interneurons
15 in the hippocampus. OLM cells can influence pyramidal (PYR) cells through two distinct pathways:
16 by direct inhibition of PYR cell distal dendrites, and by indirect disinhibition of PYR cell proximal
17 dendrites. We use previous inhibitory network models and build biophysical LFP models using
18 volume conductor theory. We examine the effect of OLM cells to ongoing intrinsic LFP theta
19 rhythms by directly comparing our model LFP features with experiment. We find that OLM cell
20 inputs regulate the robustness of LFP responses without affecting their average power and that
21 this robust response depends on co-activation of distal inhibition and basal excitation. We use our
22 models to estimate the spatial extent of the region generating LFP theta rhythms, leading us to
23 predict that about 22,000 PYR cells participate in intrinsic theta generation. Besides obtaining an
24 understanding of OLM cell contributions to intrinsic LFP theta rhythms, our work can help decipher
25 cellular correlates of *in vivo* LFPs.

26 **Significance** Oscillatory local field potentials (LFPs) are extracellularly recorded signals that are
27 widely used to interpret information processing in the brain. Theta (3-12 Hz) LFP rhythms are
28 correlated with memory processing, and inhibitory cell subtypes contribute in particular ways to
29 theta. While a precise biophysical modeling scheme linking cellular activity to LFP signals has been
30 established, it is difficult to assess cellular contributions *in vivo* to LFPs because of spatiotemporally
31 overlapping pathways that prevent the unambiguous separation of signals. Using an *in vitro*
32 preparation that exhibits theta rhythms and where there is much less overlap, we build biophysical
33 LFP models and uncover distinct inhibitory cellular contributions. This work brings us closer to
34 obtaining cellular correlates of LFPs and brain function.

36 Introduction

37 Oscillatory brain activities, as can be observed in EEGs and local field potentials (LFPs), are a ubiq-
38 uitous feature of brain recordings (*Buzsáki and Draguhn, 2004*). Accumulating evidence indicates
39 that they form part of the neural code by phasically organizing information in brain circuits (*Wilson*

40 *et al., 2015*). The LFP is the low-frequency part (<500 Hz) of the extracellular signal. Due to its
41 relative ease of recording, it is commonly used to measure neural activity. It originates from trans-
42 membrane currents passing through cellular membranes in the vicinity of a recording electrode
43 tip (*Einevoll et al., 2013*), and its biophysical origin is understood in the framework of volume
44 conductor theory (*Nicholson and Freeman, 1975*). Many sources contribute to the LFP (*Buzsáki*
45 *et al., 2012*) and depend on the frequency range of the extracellular signal. Slower oscillations (<
46 50 Hz) are generated by synaptic currents as opposed to higher frequency oscillations (> 90 Hz)
47 which are influenced by phase-modulated spiking activity (*Schomburg et al., 2012*). Determining
48 the sources of LFP output is highly challenging in general, and contributions from remote and local
49 activities can be non-intuitive (*Carmichael et al., 2017; Herreras, 2016*). In essence, it is far from
50 clear how to interpret LFP recordings in light of contributions from many different cell types and
51 pathways.

52 The hippocampus exhibits many LFP activities including theta and gamma rhythms (*Buzsáki,*
53 *2006; Colgin, 2016*). In particular, the prominent theta rhythm (3-12 Hz) is correlated with spatial
54 navigation and episodic memory, rapid eye movement sleep and voluntary behaviors (*Buzsáki,*
55 *2002*). Recently, direct behavioural relevance of theta LFP rhythm phase-coding was demonstrated
56 by delivering perturbations during specific phases of the theta rhythm to preferentially affect
57 encoding or retrieval behaviours (*Siegle and Wilson, 2014*). This was done by optogenetically
58 stimulating particular inhibitory cell types in the dorsal CA1 region of the hippocampus. Such
59 exciting studies and several reviews (*Hattori et al., 2017; Kepecs and Fishell, 2014; Klausberger*
60 *and Somogyi, 2008*) make it clear that the specifics of inhibitory cell types are fundamental to neural
61 coding and brain function. In essence, if we are to understand the brain's code, i.e., behaviour-
62 related changes in oscillatory activity, we need to understand how various cell type populations
63 contribute to LFP recordings.

64 A whole hippocampus *in vitro* preparation has been developed and spontaneously generates
65 *intrinsic* theta (3-12 Hz) rhythms (*Goutagny et al., 2009*). Given the combination of its reduced
66 nature and robust rhythms, this preparation presents an opportunity to understand cellular con-
67 tributions to LFP theta rhythms as we can remove several complicating factors by not needing
68 to consider various pathways that exist in *in vivo* scenarios. Ambiguities are greatly reduced and
69 our ability to understand cellular contributions to LFP recordings is greatly enhanced. Oriens-
70 lacunosum/moleculare (OLM) cells are a major class of GABAergic interneurons (*Maccaferri, 2005*).
71 They play an important role in gating information flow in the hippocampus by facilitating intrahip-
72 pocampal transmission from CA3 while reducing the influence of entorhinal cortical inputs (*Leão*
73 *et al., 2012*). Since OLM cells project to the distal dendrites of pyramidal cells they would be ex-
74 pected to generate large LFP deflections due to larger dipole moments (*Pettersen et al., 2012*).
75 However, these expectations may need to be modified since in addition to inhibiting distal layers
76 they can have an effect on inner and middle layers, since they inhibit interneurons that target PYR
77 cells at those layers (*Leão et al., 2012*).

78 In this paper we use computational modeling to determine the contribution of OLM cells to
79 ongoing *intrinsic* LFP theta rhythms considering their interactions with local targets using the *in vitro*
80 whole hippocampus preparation context. We take advantage of a previous modeling framework of
81 inhibitory networks (*Ferguson et al., 2015*) and generate biophysical LFP computational models,
82 and investigate the factors that influence theta LFP characteristics. By directly comparing our LFP
83 models with experiment, we are able to constrain the required connectivity profile between OLM
84 cells and other inhibitory cells types, as well as to show that OLM cells control the robustness,
85 but not the power, of intrinsic LFP theta rhythms. We are also able to assess the spatial reach
86 of the extracellular signal and so estimate the number of cells that contribute to the LFP signal.
87 In general, we show how the many complex interactions lead to emergent LFP output that are
88 non-intuitive and would not be possible to understand without biophysical LFP modeling in an
89 experimentally constrained microcircuit context. As such, our work shows a way forward to obtain
90 an understanding of cellular contributions to brain rhythms.

Figure 1. Model Setup and Experimental Essence.

A. A schematic of the network model used by *Ferguson et al. (2015)* is shown in the middle. The network model contains single compartment representations for OLM cells, BiCs, and BC/AACs. Inhibitory synapses are represented by filled black circles. Each inhibitory cell receives excitatory post synaptic currents (EPSCs) that is taken from experimental intracellular recordings as shown on the far left (adapted from *Ferguson et al. (2015)*). Each inhibitory cell synapses onto a PYR cell model as schematized. There are 350 OLM cells, 120 BiCs and 380 BC/AACs. Basal excitatory input is also included. An illustration of the polarity changes (source/sink) seen in the different labeled layers from LFP experimental recordings is shown on the right, and the detailed PYR cell morphology that is used along with the 15 equidistant electrode locations in the different layers is shown as red numbers on the far right.

B. IPSCs from the different cell types (colored as indicated) are shown on the left to show their different kinetics. Parameter values are given in Table 1, and the same coloring is used on the detailed PYR cell morphology to indicate the synaptic location regions for the different cell types. An example simulation of a computed LFP from the SR layer (using parameter values of $g_{sb}=6$ and $g_{bb}=1.25$ nS, $c_{sb}=0.21$) is shown below, and the computed current source density (CSD) is shown on the right (averaged over time). On the bottom is an example of an experimental LFP recording from the SR layer (adapted from *Ferguson et al. (2015)*).

91 **Materials and Methods**92 **Network model details**

93 This work builds on previously developed models described in *Ferguson et al. (2015)*. Here we
94 provide a summary of specifics that are salient to the present study.

95 Inhibitory cell types and numbers, pyramidal (PYR) cell model:

96 The inhibitory network model consists of 850 cells and represents a volume of 1 mm³ as shown to
97 be appropriate to obtain spontaneous theta rhythms in the *in vitro* whole hippocampus preparation
98 (*Ferguson et al., 2015, 2013; Goutagny et al., 2009*). Four different types of inhibitory cells are in-
99 cluded: basket/axo-axonic cells (BC/AACs), bistratified cells (BiCs) and OLM cells. BC/AACs comprise
100 a 380-cell population and target somatic, perisomatic and axo-axonic regions of PYR cells. The BiCs
101 comprise a 120-cell population and target middle, apical and basal regions of PYR cells, and the
102 OLM cells comprise a 350-cell population and target the distal, apical dendrites of PYR cells. As in
103 *Ferguson et al. (2015)*, the structure of the PYR cell model was based on the one used in *Migliore*
104 *and Migliore (2012)* as implemented in the NEURON Simulator (*Carnevale and Hines, 2006*) (see
105 ModelDB Accession number 144541). The PYR cell model was used as a passive integrator of inputs
106 from cell firings at the various layers of the hippocampus, and all active, voltage-gated channel
107 conductances were set to zero. This overall network model is schematized in Fig 1A. With the
108 exception of basal excitatory input, it is the same as used in *Ferguson et al. (2015)*.

109 Inhibitory cell models and drives:

110 The inhibitory cell models are single compartment, have an Izhikevich mathematical structure
111 (*Izhikevich, 2003*) and were constructed by fitting to experimental data from whole cell patch clamp
112 recordings in the whole hippocampus preparation (*Ferguson et al., 2015*). All of the cell model
113 parameter values are given in *Ferguson et al. (2015)*. Parvalbumin-expressing (PV) cell types are
114 BC/AACs and BiCs, and somatostatin-expressing (SOM) cell types are OLM cells. Each cell model
115 is driven by excitatory postsynaptic currents (EPSCs) taken directly from experiment (*Huh et al.,*
116 *2016*) during ongoing spontaneous theta rhythms for PV or SOM cells. The EPSCs were designed
117 to ensure that the inhibitory cells receive frequency-matched current inputs and at the same time
118 have amplitudes and peak alignments that were consistent with theta oscillations in experiment
119 (*Ferguson et al., 2015*) - see EPSC_{PV} and EPSC_{OLM} examples in Fig 1A. Importantly, the experimental
120 variability in amplitude and timing of EPSCs across cells was captured by varying the gain (factor
121 by which the EPSC was scaled to alter the amplitude) and timing of the EPSCs across cells with
122 a normal distribution in accordance with the experimental recordings. Thus, each inhibitory cell
123 model received a unique set of excitatory synaptic inputs reflecting the range of amplitudes and
124 timing of those recorded experimentally.

Table 1. Connectivity Parameter Values.

Cell Type X to Cell Type Y (X - Y)	Connection Probability	Maximal Synaptic Conduc.(nS) or Synaptic Weight (μ S) to PYR cell	Synaptic Rise Time (ms)	Synaptic Decay Time (ms)
BC/AAC - BC/AAC	0.12	3	0.27	1.7
BC/AAC - BiC	0.12	3	0.27	1.7
BC/AAC - OLM cell	0	N/A	N/A	N/A
BC/AAC - PYR cell	1	0.00038	0.3	3.5
BiC - BC/AAC	0.12	3	0.27	1.7
BiC - BiC	0.12	3	0.27	1.7
BiC - OLM cell	0-0.224	0-6	2	16.1
BiC - PYR cell	1	0.00044	2	16.1
OLM cell - BC/AAC	0	N/A	N/A	N/A
OLM cell - BiC	0-0.33	0-6	2	16.1
OLM cell - OLM cell	0	N/A	N/A	N/A
OLM cell - PYR cell	1	0.00067	3.5	11.8
Excitatory Input to PYR cell (197 contacts to basal tree)	1	0.00044	0.5	3

N/A = not applicable

125 Inhibitory network connectivity and output:

126 PV cells (BC/AACs and BiCs) were randomly connected with probabilities and synaptic conductance
 127 values based on experimental estimates from the literature and previous modeling work (*Ferguson*
 128 *et al., 2013*). Connections between BiCs and OLM cells are known to exist (*Leão et al., 2012*) and a
 129 range of values from the literature was previously estimated, with the connection probability from
 130 BiCs to OLM cells taken as 0.64 times the connection probability from OLM cells to BiCs (*Ferguson*
 131 *et al., 2015*). Although OLM-BiC connections exist, their synaptic conductance values are unclear
 132 but can be roughly estimated from the literature. In previous work, the balance of parameter values
 133 important for theta rhythms was specifically examined by exploring a wide range of values that
 134 encompassed determined estimates (*Ferguson et al., 2015*). Inhibitory synapses were modeled
 135 using a first order kinetic process with appropriate rise and decay time constants. The spiking
 136 output of the inhibitory network models briefly described here were computed for the range of
 137 synaptic conductance strengths and connection probabilities given in Table 1. For the work in this
 138 paper we used output from these inhibitory networks. Specifically, these simulations were done for
 139 5 seconds; the connection probability from OLM cells to BiCs (c_{sb}) varied from 0.01 to 0.33 with a
 140 step size of 0.02 producing 16 sets of connection probabilities; synaptic conductance values ranged
 141 from 0-6 nS for OLM cells to BiCs (g_{sb}) and for BiCs to OLM cells (g_{bs}). By changing g_{sb} and g_{bs}
 142 with a step size resolution of 0.25 nS, 625 raster plots were produced. So the total number of raster
 143 plots in our study here as computed in *Ferguson et al. (2015)* is (625×16) 10,000, and they are all
 144 available on Open Science Framework (osf.io/vw3jh).

145 Synaptic weights and distribution onto PYR cell:

146 Inhibitory inputs to the PYR cell model were distributed in the same way as done in *Ferguson*
 147 *et al. (2015)*. That is, we distinguished between synapses at the distal layer (stratum lacunosum-

148 moluculare), medial and basal layers (stratum radiatum and oriens), and the perisomatic/somatic
149 layer (stratum pyramidale). Distal synapses were defined as those that are $> 475\mu\text{m}$ from the
150 soma; apical and basal synapses were defined as those that are $> 50 - 375\mu\text{m}$ from the soma;
151 perisomatic/somatic synapses were defined as those that are $< 30\mu\text{m}$ from the soma. We created
152 three lists of components (where each component points to a specific segment of a section in the
153 PYR cell model), for the possible distal, proximal apical/basal, and perisomatic/somatic synaptic
154 targets. For each individual, presynaptic inhibitory cell model, we randomly chose a synaptic location
155 on the passive CA1 PYR cell model from the respective list (distal dendrites for OLM cell models,
156 apical/basal dendrites for BiC models, and perisomatic/somatic locations for BC/AACs). Then the
157 spike times from the individual, inhibitory cell models filled a vector, and an artificial spiking cell
158 was defined to generate spike events at the times stored in that vector at the specific location at
159 which that cell created a synaptic target. We used the Exp2Syn function in NEURON to define the
160 synaptic kinetic scheme of the synapse. This function defines a synapse as a synaptic event with
161 exponential rise and decay, that is triggered by presynaptic spikes, and has a specific weight that
162 determines its synaptic strength, and an inhibitory reversal potential of -85 mV , as measured in the
163 whole hippocampus preparation. Synaptic weight values onto the PYR cell from the different cell
164 populations were estimated using somatic IPSC values for OLM cells onto PYR cells (*Maccaferri et al.,*
165 *2000*). As these synaptic weights were not clearly known, we used different synaptic weight profiles
166 in the explorations as was been done previously (*Ferguson et al., 2015*). The main profile used
167 was graded such that the different cell types led to similar somatic IPSC amplitudes, considering
168 that $0.00067\ \mu\text{S}$ can be estimated from the OLM cells IPSC currents (see Table 1). Several other
169 synaptic weight profiles were examined. Finally, we note that an ad-hoc representation for LFPs
170 was previously used (*Ferguson et al., 2015*) as given by an inverted summation of all integrated
171 inputs as measured at the PYR cell soma. That is, the postsynaptic potentials on the PYR cell were
172 due to the various inhibitory cell firings that comprised the presynaptic spike populations.

173 **Additional network model details for this study**

174 For the study here, inhibitory inputs were distributed in the same way as in *Ferguson et al. (2015)*.
175 In *Ferguson et al. (2015)* the literature was used to estimate synaptic conductances between OLM
176 cells and BiCs as 3-4 nS, and *Bezaire et al. (2016)* used 10 synapses/connection as estimates in their
177 detailed data-driven computational models. This implies that a single synapse would be 0.3-0.4 nS,
178 representing an approximate minimum connection weight.

179 As we made direct comparisons with theta LFP experimental recordings here, it was important
180 to include excitatory input to the PYR cell model. Thus we also included excitation due to CA1
181 recurrent collaterals which synapse on basal dendrites (*Takács et al., 2012*). In *Ferguson et al.*
182 *(2015)* excitatory feedback was not included in a direct fashion as the focus was on ongoing theta
183 rhythms and OLM-BiC interactions, and not on theta generation mechanisms explicitly. Thus,
184 model excitatory cell populations were not specifically modelled. This means that we did not
185 have explicit spike rasters for excitatory populations as we did for the inhibitory cell populations.
186 Rather than generate an arbitrary set of spike times to simulate excitatory inputs, we used spike
187 times from a BiC raster ($g_{sb}=3.75$, $g_{bs}=1.75\text{ nS}$, $c_{sb}=0.21$) in which the neuron order was randomized,
188 and with comparable synaptic weights. Using these random spike trains we generated spike
189 vectors exactly as in the case of interneurons and randomly distributed them on basal dendrites
190 using 197 synapses based on number estimates from *Bezaire and Soltesz (2013)* and *Bezaire et al.*
191 *(2016)*. In this way, we did not have a spatiotemporal dominance of inhibitory or excitatory input
192 in basal dendrites. We used an excitatory reversal potential of -15 mV as measured in the whole
193 hippocampus preparation, and synaptic time constants in line with modeling work (*Ferguson et al.,*
194 *2017*). In essence, we simulated EPSCs using random spike trains of theta frequency instead of
195 explicitly modeling pyramidal cell spiking activity. We note that with these choices, somatically
196 recorded currents in our PYR cell models were similar to what is observed in experiments (*Huh*
197 *et al., 2016*). All parameter values are summarized in Table 1.

198 We note that the inhibitory cell spike rasters computed in *Ferguson et al. (2015)* used random
 199 connectivities between the different inhibitory cell populations. Consider that a given set of
 200 parameters (c_{sb}, g_{sb}, g_{bs}) defines a connectivity map. Each cell within a given population is randomly
 201 assigned a synaptic location within the boundaries of the dendritic tree on which it projects. Based
 202 on a given connectivity map the spiking activity of the various cell populations will differ. Therefore
 203 the characteristics of the produced biophysical LFP will depend on the spike distribution of a given
 204 population defined by the connectivity map and also the number and location of synapses on the
 205 dendritic tree. To ensure that our LFP output was not dependent on the specific synaptic location
 206 that every cell was assigned to, we generalized our observations by performing many trials for a
 207 given connectivity map, assigning randomly different location to the cells of each population to
 208 ensure that the LFP output was not dependent on that aspect.

209 Biophysical computation of LFP

210 Extracellular potentials are generated by transmembrane currents (*Nunez and Srinivasan, 2006*).
 211 In the commonly used volume conductor theory, also used here, the extracellular medium was
 212 modeled as a smooth three-dimensional continuum with transmembrane currents representing
 213 volume current sources. The fundamental formula (*Pettersen et al., 2012*) relating neural activity in
 214 an infinite volume conductor to the generation of the LFP $\phi(r, t)$, at a position r is given by:

$$\phi(r, t) = \frac{1}{4\pi\sigma} \sum_{k=1}^n \frac{I_k(t)}{|r - r_k|} \quad (1)$$

215 Here I_k denotes the transmembrane current (including the capacitive current) in a neural compart-
 216 ment k positioned at r_k , and the extracellular conductivity, here assumed real (ohmic), isotropic
 217 (same in all directions) and homogeneous (same at all positions), is denoted by σ . In the hippocam-
 218 pus the mean extracellular conductivity σ is equal to 0.3Sm^{-1} (*López-Aguado et al., 2001*) which
 219 is the value that we used for our simulations. A key feature of Equation 1 is that it is linear, i.e.,
 220 the contributions to the LFP from the various compartments in a neuron sum up. Likewise the
 221 contributions from all the neurons in a population would add up linearly. The transmembrane
 222 currents I_k setting up the extracellular potentials according to Equation 1 were calculated by means
 223 of standard multi-compartment modeling techniques, here by use of the simulation tool NEURON
 224 *Carnevale and Hines (2006)*. The current source densities (CSDs) in Fig 1B were computed using
 225 the 1D kCSD inverse method proposed in *Potworowski et al. (2012)*. The CSDs were computed
 226 from the LFP measured by electrodes that are arranged along a straight line, in this case along the
 227 cellular axis of the PYR cell.

228 The same PYR cell multi-compartment model as described above was used to compute the
 229 extracellular biophysical LFP, and we used the set of 10,000 5-second raster plots (of inhibitory
 230 spikes) as described above for our presynaptic populations with the addition of basal excitation.
 231 That is, we generated extracellular potential traces (5 sec each) due to the various inhibitory cell
 232 firings. We used a single multi-compartment PYR cell to compute the biophysical LFP. While an
 233 experimental LFP is generated by many cells, we still referred to our extracellular output as an
 234 'LFP' for consistency with the computational literature, where the 'LFP' term has been used for an
 235 extracellular field from single or multiple cells.

236 Simulation details

237 The computational simulations and analyses were performed using the LFPy python package
 238 **RRID:SCR_014805** (*Lindén et al., 2014*), NEURON **RRID:SCR_005393** (*Carnevale and Hines, 2006*)
 239 and MATLAB **RRID:SCR_001622** (MATLAB 8.0 and Statistics Toolbox 8.1). The large scale network
 240 simulations were conducted using high-performance computing at SciNet *Loken et al. (2010)*. The
 241 code/software described in the paper is freely available online at [URL redacted for double-blind
 242 review]. The code is available as Extended Data.

243 Results

244 **Intrinsic theta rhythms in the hippocampus**

245 It has long been known that input from the medial septum is an important contributor to *in vivo* LFP
246 theta rhythms (Buzsáki, 2002). However, recent work by Goutagny *et al.* (2009) showed that theta
247 rhythms can emerge in the CA1 region of an intact *in vitro* hippocampus preparation. These *intrinsic*
248 theta rhythms appeared spontaneously without any pharmacological manipulations or artificial
249 stimulation paradigms, and persisted even after the neighboring CA3 subfield was removed. It is
250 thus clear that intrinsic theta frequency rhythms can be produced by local interactions between
251 interneurons and PYR cells in the hippocampus. That is, the CA1 region of the hippocampus
252 contains sufficient circuitry to be able to generate theta oscillations. An example of this intrinsic LFP
253 rhythm is shown in Fig 1B. Considering this preparation, a one cubic millimetre estimate of the tissue
254 size (i.e., network circuitry) needed for intrinsic theta rhythm to occur was estimated (Ferguson
255 *et al.*, 2013). While it is clear that these intrinsic theta rhythms do not fully encompass *in vivo* theta
256 rhythms, they undoubtedly exist without any special manipulations, and so are arguably part of the
257 underlying biological machinery generating theta rhythms in the hippocampus. More importantly,
258 to have a chance to understand the many different cellular contributions to LFP recordings, this
259 preparation can be used to decipher the many interacting components.

260 To examine the role of specific hippocampal interneurons in these intrinsic theta rhythms,
261 Amilhon *et al.* (2015) optogenetically activated and silenced PV or SOM interneurons. PV cell
262 types exhibiting fast firing characteristics include basket cells (BCs), axo-axonic cells (AACs) and
263 bistratified cells (BiCs) (Baude *et al.*, 2007). OLM cells are SOM-positive but it is not the case that
264 SOM interneurons are necessarily OLM cells. However, reconstructions of SOM cells in these studies
265 with intrinsic theta were done, confirmed that they were likely OLM cells (Huh *et al.*, 2016). Amilhon
266 *et al.* (2015) found that optogenetic manipulation of SOM cells modestly influenced the intrinsic
267 theta rhythms. In contrast, activation or silencing of PV cells strongly affected theta. These results
268 thus demonstrated an important role for PV cells but not SOM cells for the emergence and presence
269 of intrinsic hippocampal theta, as given by the observed LFP recordings exhibiting theta rhythms.

270 LFP recordings in this preparation had a particular sink and source distribution in the different
271 layers (Goutagny *et al.*, 2009). It is given by a single dipole characterized by positive deflections
272 in stratum lacunosum/moleculare (SLM) and stratum radiatum (SR) and negative deflections in
273 stratum pyramidale (SP) and stratum oriens (SO). The dipole is illustrated in Fig 1A. This LFP laminar
274 polarity profile was consistent across preparations. We note that since theta rhythms persisted
275 even when the CA3 region was removed, excitatory collaterals from CA3 did not seem to be a
276 necessity for the emergence of the rhythm and the sink/source density profile. Thus, in our LFP
277 model in this work, we assumed that excitatory input to CA1 pyramidal (PYR) cells was restricted to
278 the basal dendrites due to CA1 PYR cell collaterals (Goutagny *et al.*, 2009).

279 **Using a previous network model framework as a basis**

280 To try to understand how the complex interactions between different inhibitory cell types con-
281 tributed to theta LFP rhythms, a computational network framework representing CA1 microcircuitry
282 was previously developed (Ferguson *et al.*, 2015). Given the ambiguous role of OLM cells in theta
283 rhythms and the newly discovered connections between OLM cells and BiCs (Leão *et al.*, 2012),
284 these network models were developed to explore how OLM-BiC interactions influenced the charac-
285 teristics of theta rhythms. We took advantage of previously developed PV fast-firing cell models
286 (Ferguson *et al.*, 2013) and OLM cell models (Ferguson *et al.*, 2015) based on recordings from the
287 whole hippocampus preparation. Because of distal contacts of OLM cells with PYR cells, a multi-
288 compartment PYR cell model was previously used to be able to incorporate this aspect in exploring
289 the various interactions. The network model framework is shown in Fig 1A and a summary of the
290 network model is provided in the Methods. We note that the network model was designed to
291 explore cellular interactions and contributions to the ongoing intrinsic theta rhythms, and not to

292 the generation of the theta rhythms explicitly. All inhibitory neurons were driven by theta frequency
293 inputs based on experimental recordings from the whole hippocampus preparation.

294 As schematized in Fig 1A, the inhibitory cell populations encompassed BC/AACs, BiCs and OLM
295 cells that were driven by experimentally-derived EPSCs. These EPSCs were from the ongoing rhythm
296 and were of theta frequency (see Fig 1A). Spiking output from the inhibitory cell populations led
297 to inhibitory postsynaptic currents (IPSCs) on the PYR cell. They were distributed on the PYR cell
298 according to where the particular cell population targeted. Thus, BC/AACs to somatic regions, BiCs
299 to middle apical and basal regions and OLM cells to distal apical regions. IPSCs generated by the
300 different cell types are shown in Fig 1B (see Methods for details). In previous work, the spatial
301 integration of the inhibitory postsynaptic potentials at the soma of a passive PYR cell model was
302 used as a simplistic LFP representation (Ferguson et al., 2015). This representation was in fact
303 indicative of the intracellular somatic potential rather than the extracellular one, but it did allow the
304 distal OLM cell inputs relative to more proximal PV cell inputs to be taken into consideration. Using
305 this computational model framework, multiple simulations were performed and it was shown that
306 there were parameter balances that resulted in high or low theta power, and where OLM cells did or
307 did not affect the theta power (Ferguson et al., 2015). That is, OLM cells could play a small or large
308 role in the resulting theta power depending on whether compensatory effects with BiCs occurred as
309 a result of the size and amount of synaptic interactions between these cell types. Thus, interactions
310 between OLM cells and BiCs in the CA1 microcircuitry seemed to be an important aspect for the
311 presence of intrinsic LFP theta rhythms. However, since an ad-hoc LFP representation was used, it
312 was not possible to do any direct comparisons with experimentally recorded LFPs to decipher their
313 output. That is, the possibility to parse out the contribution of the different cell types or identify
314 particular interactions was limited. Thus, while it was possible to show that interactions between
315 OLM cells and BiCs could play an essential role in the resulting theta power, it was not possible to
316 predict any particular parameter balances or to extract possible explanations.

317 In the work here, we built on this model framework and developed biophysical LFP models.
318 We used the inhibitory spiking output generated in Ferguson et al. (2015) as a basis for generating
319 biophysical LFPs, and we used the same PYR cell model. However, unlike the previous work, we
320 used the framework of volume conductor theory (see Methods) and generated actual extracellular
321 potential output as a result of the overall activity of the inhibitory cell firings across the various layers
322 of CA1 hippocampus. In addition we included excitatory input onto the basal dendrites to represent
323 recurrent CA1 inputs (see schematic in Fig 1A and Methods for details) and directly compared with
324 characteristics of experimental LFP recordings. It is important to note that the structure of our
325 model here did not focus on deciphering the generation of theta rhythms directly. Rather, there was
326 the point neuron network model with the inhibitory cells receiving theta-frequency EPSC inputs and
327 the multi-compartment PYR cell model generating biophysical LFP output based on the synaptic
328 inputs it was receiving. In this way, we were able to do extensive parameter explorations and to
329 focus on comparing model and experimental LFPs to gain insight.

330 **Overall characteristics of biophysical LFP models**

331 From the previous modeling study of Ferguson et al. (2015), several sets of inhibitory spiking output
332 with particular connection probabilities and particular synaptic conductances between OLM cells
333 and BiCs were available. The connection probability from OLM cells to BiCs (c_{sb}) varied from 0.01 to
334 0.33 with a step size of 0.02 producing 16 sets of connection probabilities; synaptic conductance
335 values ranged from 0-6 nS for OLM cells to BiCs (g_{sb}) and for BiCs to OLM cells (g_{bs}) with a step
336 size of 0.25 nS. Thus, for a given connection probability, there were 625 sets of spiking outputs
337 from inhibitory cells, where each set represented a 850-cell inhibitory network with particular
338 synaptic conductances. We considered a set to be a connectivity map representing the inhibitory
339 cell populations.

340 For each connectivity map, we generated a biophysical, extracellular LFP. A virtual electrode
341 probe was placed along the vertical axis of the PYR cell model to record its LFP output in a layer

Figure 2. Biophysical LFP Computation: Features, Examples and Interneuron Activities.

A. (i) Schematic shows 2 raster plot examples for the given inhibitory cell population rasters. **(ii)** The resulting LFPs at the somatic layer, with positive and negative deflections is shown for the examples, labelled with dark- or light-colored squares. Parameter values are $g_{sb}=1.5$, $g_{bs}=5.5$ nS for positive and $g_{sb}=0.5$, $g_{bs}=0.75$ nS for negative deflections. **(iii)** The color plot on the right shows the polarity at the somatic layer, SP, electrode 4. Dotted lines delineate 4 regions labelled as a, b, c, d. Negative polarity: dark-colored squares, positive polarity: light-colored squares. **(iv)** LFP output for all layers are shown for 3 examples where the polarity is negative, positive and negative at electrode 3 (left to right). Parameter values are (left to right): $g_{sb}=0.5$, $g_{bs}=0.75$; $g_{sb}=1.5$, $g_{bs}=5.5$; $g_{sb}=5.75$, $g_{bs}=0.75$ nS. Inset shows a blow up of LFP output at electrode 13 (SLM) to show positive deflections. Also shown is the intracellular somatic potential of the PYR cell. No basal excitation is present, $c_{sb}=0.21$.

B. (i) Schematic includes 1 raster plot example. **(ii)** The resulting LFP output at SP has 5 peaks. A maximum of 29 peaks is possible (see text). Parameter values are $g_{sb}=2$, $g_{bs}=0.75$ nS. **(iii)** The color plot shows the number of peaks that appear in the 5-second LFP computation at SP, electrode 4. Dotted lines delineate the same regions as in A. **(iv)** An example of LFP output for all layers as well as the intracellular somatic output which also shows a loss of peaks. Parameter values are $g_{sb}=2.25$, $g_{bs}=5.0$ nS. No basal excitation is present, $c_{sb}=0.21$.

C. Interneuron activity for each interneuron population, normalized such that the number of spikes for a given pair of synaptic conductances is divided by the maximal number considering all pairs of synaptic conductances. Maximal number (5-second trace): 16,327 (BC/AACs), 6,808 (OLM cells), 4,589 (BiCs).

342 dependent manner. This PYR cell model was the “processor” of the LFP signal as it integrated post-
 343 synaptic inputs from different presynaptic populations. We computed LFPs at 15 equidistant sites
 344 along a linear axis - see Fig 1A. The PYR cell output corresponded to readouts of the postsynaptic
 345 activity elicited by the afferent inhibitory cell populations that targeted the PYR cell in appropriate
 346 regions, referred to as the LFP “generator”. We note that although there was a single connectivity
 347 map representing the randomly connected inhibitory cell population, we performed several trials
 348 when randomly targeting the PYR cell to ensure the robustness of our results (see Methods). To
 349 achieve effective electroneutrality, the extracellular sink needed to be balanced by an extracellular
 350 source, that is, an opposing ionic flux from the intracellular to the extracellular space, along the
 351 neuron; this flux was termed the ‘return current’.

352 We developed some initial intuition regarding the generation of our biophysical LFPs by comput-
 353 ing them *without* including basal excitation. That way, all of the inputs received by the PYR cell model
 354 were inhibitory. Fig 2A,B illustrates the process and shows some examples. Let us first focus on Fig
 355 2A(i). Next to each cell population in the network schematic are two examples of 1-second raster
 356 plots of spiking outputs (from the previously computed 5-second inhibitory network simulations in
 357 *Ferguson et al. (2015)*) produced for particular parameter sets. These spikes gave rise to IPSCs on
 358 the PYR cell model and the computed extracellular LFP at the somatic layer is shown in Fig 2A(ii). As
 359 shown, these particular parameter sets produced LFPs with positive or negative deflections. Let us
 360 next focus on Fig 2B(i). One example of a 1-second raster plot is shown, and for this parameter set,
 361 the LFP had only a few positive deflections, as shown in Fig 2B(ii). Assuming that one population
 362 burst in the raster plot leads to a single peak in the LFP, there would be about 29 peaks in the
 363 LFP for a 5-second simulation (i.e., about 5.8 Hz frequency) since our inhibitory cell raster plots
 364 have 28-29 population bursts. Note that the raster plots in Fig 2B(i) were not very different from
 365 the examples shown in Fig 2A(i). We computed LFPs at all layers as represented by the 15 virtual
 366 electrodes shown in Fig 1A for the 625 sets of inhibitory spiking outputs across g_{sb} and g_{bs} values at
 367 a particular connection probability c_{sb} . The colored plot in Fig 2A(iii) shows the polarity of the LFPs
 368 at the somatic layer, and the color plot in Fig 2B(iii) shows the number of LFP peaks in the somatic
 369 layer. In Fig 2C normalized spike numbers for all interneuron populations are shown.

370 As a first approximation, given the network model framework and previous work we can say the
 371 following about the LFPs: Those governed mainly by synaptic inputs and not return currents were
 372 characterized by narrow waveform shapes as the synaptic inputs from any particular interneuron
 373 population enters the PYR cell in a synchronized fashion. This was due to the inhibitory cells in
 374 a given population being driven by rhythmic EPSCs that gave rise to coherently firing inhibitory
 375 cells in a given population (see example raster plots). We note that the EPSCs that were used in

376 the simulations were not perfectly synchronized since the measured experimental variability was
377 included in designing the EPSC inputs to use in the inhibitory network simulations (see Methods).
378 On the other hand, return currents constituted a summation of less synchronized exiting currents
379 that originally entered the cell at different locations. Therefore, LFP deflections governed by return
380 currents were generally wider. Further, we would expect that the LFP recorded from different layers
381 would first and foremost be influenced by the interneurons that project to that region. We also
382 note that the width of the LFP deflection would not only be influenced by the nature of the current
383 (synaptic inputs or return currents) but also by the synaptic time constants defining the shape of
384 the IPSCs. IPSCs for the different cell populations are shown in Fig 1B where it can be seen that the
385 IPSCs produced by OLM cells and BiCs were wider relative to the IPSCs from BC/AACs. Thus, we
386 expected that positive LFP deflections would be recorded in locations where OLM cells, BiCs and
387 BCs project, with wider LFPs for OLM cell projection locations, and that LFPs dominated by return
388 currents would be recorded in locations where there were no direct inputs from interneurons.
389 However, due to interactions between BiCs and OLM cells, this was not necessarily the case as
390 return currents from distant interneuronal inputs could prevail in regions where other interneurons
391 directly projected. In fact, interactions between OLM cells and BiCs can strongly modulate the
392 relative balance between synaptic inputs and return currents, which in turn can strongly modulate
393 the distribution of sinks and sources in the resulting LFP.

394 The two examples of LFP output at the somatic layer in Fig 2A(ii) show one with narrow positive
395 deflections and the other with wider negative deflections. This thus indicated that the BC/AAC
396 inputs that synapse at the somatic layer dominated for the positive deflection LFP example whereas
397 BiC and OLM cell inputs that synapse more distally dominated for the negative wider deflection
398 LFP example. The example in Fig 2B(ii) of LFP output at the somatic layer indicated that a loss of
399 peaks can occur due to the superposition of synaptic inputs and return currents. Another “loss of
400 peaks” example is shown in Fig 2B(iv), and LFP output from multiple layers is shown in addition to
401 the intracellular somatic output. For this example, the peak loss was also partially reflected in the
402 intracellular somatic output. However, loss of peaks in the LFP output was not necessarily reflected
403 in the somatic intracellular recording. Note that since the PYR cell was only receiving inhibitory input
404 in these set of simulations, somatic intracellular potentials always had negative deflections. How
405 the extracellular potential features changed as a function of the synaptic conductances between
406 BiCs and OLM cells is summarized in the color plots of Fig 2A(iii) for the polarity and Fig 2B(iii) for
407 the number of peaks (somatic layer).

408 Let us consider Fig 2A(iii). We found that we can approximately distinguish four regions as g_{sb}
409 was increased. These regions are separated by dotted lines in Fig 2A(iii) and labelled a to d . For
410 small g_{sb} values (0-1 nS, region a) the amount of inhibition that the BiCs received from the OLM
411 cells was minimized allowing the BiCs to be at the peak of their activity (see Fig 2C). Consequently,
412 the inhibition that the OLM cells and BC/AACs received from the BiCs was maximized causing their
413 activities to be minimized (see Fig 2C). As a result, the extracellular potential in the somatic region
414 was governed by return currents leading to negative polarity LFPs in the somatic layer (i.e., mainly
415 dark-colored in region a of Fig 2A(iii)), primarily due to the BiC synaptic inputs on the ‘middle’ region
416 (SR layer) and ‘basal’ region (SO layer) of the PYR cell. As we increased g_{sb} (1-3.5 nS, region b), we
417 encountered mainly positive polarity LFPs (i.e., light-colored in region b of Fig 2A(iii)). In region b , the
418 inhibition onto the BiCs was increased and thus their activity was decreased, as can be seen in Fig
419 2C, causing a decrease in the amount of the inhibitory current onto the PYR cell from BiCs. As a
420 result, the magnitude of the return currents caused by the BiC synaptic inputs was decreased at the
421 somatic layer. Simultaneously their ability to inhibit the BC/AACs was also decreased so that the
422 BC/AACs became more active and their direct inhibition onto the PYR cell also increased. Since both
423 BiCs and OLM cells activity was low in region b while BC/AAC activity was increased, the somatic LFP
424 was governed by BC/AAC inputs rendering the extracellular LFP positive. As we further increased
425 g_{sb} (3.5-5 nS, region c) the silencing of the BiCs increased even further and their ability to silence
426 the BC/AACs was further reduced. Simultaneously OLM cell activity increased. Thus the somatic

427 LFP was influenced by direct synaptic inputs from BC/AACs and also return currents from OLM
428 cells (sparse dark-coloring region *c*). Interestingly, the majority of the “loss of peaks” in somatic
429 LFP output occurred in regions *b* and *c* (see blue-green pixels in the Fig 2B(iii)) where superposition
430 of synaptic inputs and return currents was mostly occurring. That is, cancellations occurred even
431 leading to abolishment of the entire rhythm sometimes. Finally, for g_{sb} from 5.0-6 nS (region *d*), the
432 BiCs were maximally inhibited and BC/AACs were at the peak of their activity. While we might have
433 expected domination from the BC/AAC synaptic inputs for these values, it turns out that return
434 currents (negative polarity) dominated. This can be explained by the increased activity of OLM cells
435 which were also at the peak of their activity producing strong return currents in the somatic region.
436 In summary, light-colored regions in Fig 2A(iii) signify that BC/AACs dominated the extracellular
437 somatic potential and dark-colored regions signify that other inhibitory cell types (BiCs or OLM cells,
438 or both) contributed more strongly.

439 In Fig 2A(iv), we show three examples of LFP recordings at multiple layers as well as the somatic
440 intracellular potential, for increasing values of g_{sb} from left to right. To allow an appreciation of the
441 changing magnitude of the signal, we used the same resolution on the ordinate axis for all LFP plots
442 shown. On the left ($g_{sb}=0.5$ nS) we see that the signal was governed by return currents (negative
443 polarity) in the entire SP (electrodes 3 and 5), in SO (electrode 1) and in SR (electrodes 7,9 and 11).
444 Synaptic events governed SLM (electrodes 13 and 15) where OLM cells directly project leading to
445 positive polarity. In the middle ($g_{sb}=1.5$ nS), the LFP in SP and SO was governed by synaptic inputs
446 (positive polarity), and in SR and SLM by return currents (negative polarity). As expected, we found
447 that the positive polarity LFP in SP here was narrower relative to the positive polarity LFP in SLM
448 on the left, because the IPSCs produced by OLM cells were wider relative to those of BC/AACs, as
449 shown in Fig 1B. On the right where $g_{sb}=5.75$ nS, we observed a similar trend as for the example on
450 the left where $g_{sb}=0.5$ nS with return currents dominating.

451 We would like to use our computational LFPs to determine how the different inhibitory cell types
452 contributed to theta LFPs as recorded experimentally in the *in vitro* whole hippocampus preparation.
453 As described above, our overall network model (Fig 1A) was intended to capture an intrinsic theta
454 rhythm in the CA1 region of the *in vitro* preparation. CA3 input was not required but local excitatory
455 input which occurs on basal dendrites (Takács *et al.*, 2012) did need to be included. To do this, we
456 took advantage of previous modeling studies (Bezaire and Soltesz, 2013; Ferguson *et al.*, 2015) as
457 detailed in the Methods. Including excitatory input would clearly affect resulting biophysical LFP
458 outputs. Specifically, the LFP amplitude in SO might decrease even further in the presence of basal
459 excitation as excitatory and inhibitory BiC inputs could cause mutual cancellations in this region. As
460 return currents mostly exit close to the somatic region where the surface area is larger, the effect of
461 basal excitation might be stronger in SO and SP since most of the current might have exited before
462 reaching SR and SLM. In general, we expect there to be a range of possible LFP characteristics
463 based on the above LFP computations done in the absence of basal excitation. We expect that
464 the addition of excitatory input will influence the LFP in non-intuitive and nonlinear ways and the
465 intuition developed above will be helpful in deciphering and explaining the contribution of the
466 different cell populations to the LFP.

467 **Constraining synaptic conductances and connection probabilities between BiCs** 468 **and OLM cells**

469 In this work we focused mainly on OLM cells. The previous model network framework (Ferguson
470 *et al.*, 2015) was developed based on knowing that connections exist between BiCs and OLM cells
471 (Leão *et al.*, 2012). Given this, there were two pathways to consider for how OLM cells could
472 influence ongoing intrinsic theta LFP rhythms. They can influence LFP output indirectly through
473 disinhibition of proximal/middle dendrites of the PYR cell (OLM-BiC-PYR, indirect pathway), or
474 directly through inhibition of distal, apical dendrites of the pyramidal cell (OLM-PYR, direct pathway).
475 As shown above, many different LFP features can be exhibited in the absence of basal excitation
476 (see Fig 2A,B). It is interesting to note that our biophysical LFP output did not necessarily exhibit

Figure 3. Example LFPs from Selected and Rejected Parameter Sets.

Computed LFPs are shown across multiple layers. **Top:** Selected parameter set: $g_{sb}=6$, $g_{bs}=1.25$ nS. **Bottom:** Rejected parameter sets (left to right): $g_{sb}=0.5$, $g_{bs}=0.75$ nS; $g_{sb}=0.5$, $g_{bs}=3.5$ nS; $g_{sb}=2.5$, $g_{bs}=1$ nS. $c_{sb}=0.21$ for all.

Figure 4. All Selected and Rejected Parameter Sets.

Parameter sets are considered as selected (purple) if computed LFPs match LFPs from experiment in polarity and frequency (3 Hz lower bound). Otherwise, as rejected (yellow). A clear separation in parameter space occurs for $c_{sb} = 0.21$.

477 theta frequencies, despite being driven by theta frequency EPSC inputs (see Fig 2B(ii)). This is
 478 because cancellations in the extracellular space between synaptic inputs and return currents can
 479 result in loss or even abolishment of the rhythm. This underscores the importance of modeling
 480 biophysical LFPs as the interaction of synaptic and return currents on the extracellular signal can
 481 strongly affect the resulting LFP frequency.

482 We proceeded to include basal excitation and performed a full set of computations for all
 483 connection probabilities (c_{sb}) and synaptic conductances (g_{sb} , g_{bs}). With these computed biophysical
 484 LFPs in hand, we did direct comparisons with experimental LFPs from the whole hippocampus
 485 preparation *in vitro*. Specifically, we classified each set of network parameters as *selected* or *rejected*
 486 based on whether our computed LFPs were able to reproduce two robust characteristics exhibited
 487 experimentally. These were: (i) the laminar polarity profile exhibited a single dipole with sinks in
 488 the basal dendrites and sources in the apical dendrites, and (ii) the frequency of the LFP traces
 489 across all layers was in the theta frequency range. These characteristics are shown in Fig 1A. We
 490 note that our model setup in which experimentally-derived theta frequency EPSCs were input to
 491 the inhibitory cells means that the LFP rhythm should have a theta frequency. However, as we have
 492 shown above, the resulting biophysical LFP frequency can be much less than theta due to synaptic
 493 and return current interactions and cancellations (see Fig 2B(ii)). Specifically, the frequency of the
 494 EPSCs used from experiment is about 5.8 Hz. Thus, in enforcing the theta frequency on our LFP
 495 computations, it was only necessary to impose a lower bound. We used 3 Hz as the lower bound
 496 for theta range to be similar to experiment (Goutagny *et al.*, 2009). We applied a peak detection
 497 on the LFP trace and used a threshold to avoid detecting baseline peaks. We required that the
 498 number of peaks be larger than 15 which given the 5 sec LFP trace corresponds to 3 Hz. In Fig 3
 499 (top) we show an example of computed LFPs across the different layers for a parameter set that
 500 was selected. The bottom of Fig 3 shows LFP outputs for three different parameter sets that were
 501 rejected - incorrect polarities and frequencies are apparent. Note that ordinate resolutions were
 502 adjusted across the layers so that the frequency and polarity of computed LFPs can be readily seen
 503 in each layer in viewing.

504 Classifying each parameter set, we summarize our results in Fig 4 where selected parameter
 505 sets are shown in purple and rejected ones in yellow. We observed the following: For low c_{sb} , the
 506 plots have a checkered appearance since small changes in g_{sb} and g_{bs} caused the system to alternate
 507 between being selected or rejected. As c_{sb} increased, there was a clearer separation in (g_{sb} , g_{bs})
 508 parameter space of selection or rejection. This was observed from $c_{sb}=0.19$ to $c_{sb}=0.25$. In this
 509 range, we considered the system to be robust as it was not very sensitive to synaptic conductance
 510 perturbations. However, for $c_{sb}=0.19$, 0.23 and 0.25, the selected parameter sets were quite narrow.
 511 As c_{sb} was further increased, the checkered patterning returned. Note that the selected sets were
 512 mainly affected in one direction as c_{sb} changed. That is, across g_{sb} rather than g_{bs} values. Further,
 513 we note that in doing this classification, it was more the polarity criteria rather than the frequency
 514 criteria of the LFP signal that delineated selected and rejected parameter sets. This is shown in Fig
 515 5 where we did not apply any frequency bound or used different lower frequency bounds. While
 516 there was some change in selected and rejected parameter sets, they were minimal.

517 Since there is natural variability in biological systems, we assumed that sensitivity to small

Figure 5. Selected and Rejected Parameter Sets Using Different Lower Frequency Bounds.

The different frequency bounds used are shown at the top of each column and only 3 different c_{sb} values are shown. Note that we use 3 Hz as the frequency bound in Fig 4.

Figure 6. Predicted Regime.

For $c_{sb} = 0.21$, selected parameter sets (purple) include g_{sb} values of 3.5-6 nS, and all g_{bs} values. Rejected sets are in purple. On the right are LFP traces from 8 electrodes for a parameter set of $g_{sb} = 4.75$, $g_{bs} = 4.50$ nS.

518 perturbations in parameter values is anathema to having robust LFP theta rhythms. Noting that
 519 the synaptic conductance resolution in our simulations was 0.25 nS, and that a minimal synaptic
 520 weight can be estimated as larger than this (see Methods), we considered that (g_{sb} , g_{bs}) parameter
 521 sets that did not yield at least two complete, consecutive rows or columns of purple (selected) were
 522 inappropriate for the biological system. That is, variability that was less than a minimal synaptic
 523 weight would not make sense. Looking at this in Fig 4, we first note that there was never at least two
 524 complete purple rows for any c_{sb} , but there were cases of two or more complete purple columns,
 525 namely, $c_{sb}=0.03$ and 0.21. However, a complete purple column for $g_{sb}=0$ was invalid since it is
 526 known that OLM to BiC connections exist *Leão et al. (2012)*. Thus, $c_{sb}=0.03$ can be eliminated leaving
 527 $c_{sb}=0.21$ as appropriate. For this connection probability, the transition from selected to rejected
 528 networks and vice versa strongly depended on g_{sb} rather than on g_{bs} values, revealing a more
 529 important role for the former. In summary, by directly comparing characteristics of our computed
 530 biophysical LFPs with those from experiment, we were able to constrain an appropriate connectivity
 531 as $c_{sb}=0.21$, with g_{sb} values of 3.5 to 6 nS, and the full set of g_{bs} values ($g_{sb} \neq 0$, $g_{bs} \neq 0$). We will refer
 532 to this set of parameter values as the *predicted regime*. In Fig 6 we show example LFP responses
 533 across several layers for a set of parameter values from this *predicted regime*.

534 **OLM cells ensure a robust theta LFP signal, but minimally affect LFP power, and**
 535 **only through disinhibition**

536 In continuing our analysis, we now focused on constrained parameter sets as determined above
 537 which we termed the *predicted regime* ($c_{sb}=0.21$). We decomposed the signal to be able to examine
 538 the contribution of the interneuron subtypes to the power of the LFP. We separated our interneuron
 539 subtypes into two groups - PV subtypes which are BC/AACs and BiCs, and SOM subtypes which
 540 consist of the OLM cells here. These two groups were represented by distinct mathematical
 541 models of fast-firing PV and SOM inhibitory cells based on whole cell recordings from the whole
 542 hippocampus preparation (*Ferguson et al., 2015*). We performed spectral analyses of our computed
 543 LFPs and used the peak amplitude as a measure of the power of the theta network activity. The peak
 544 power was computed for each of the 15 electrodes (i.e., all layers), and we plotted the maximum
 545 value from all of the layers in the color plots of Fig 7. This is illustrated on the right of Fig 7A. We
 546 first simulated the spectral LFP power when all presynaptic inhibitory cell populations were present.
 547 As shown in Fig 7A, a robust power feature emerged. When all presynaptic origin populations were
 548 present, the predicted regime shown in purple in Fig 6, produced LFP responses whose power
 549 showed minimal variability. This is an interesting observation on its own, as the power of the
 550 LFP varied little across hippocampus preparations (*Goutagny et al., 2009*). Thus, our predicted
 551 regime satisfied another characteristic of experimental LFPs. We note that outside of the predicted
 552 regime, the LFP output showed much more variability, and the LFP frequency across layers was not
 553 necessarily theta, as it was not part of the selected parameter sets. For completeness, we show
 554 peak power computations that were done for all connectivities in Fig 8.

555 To examine the role of presynaptic origin populations on the LFP we decomposed the signal by
 556 selectively removing OLM to PYR cell connections or PV to PYR cell connections and then computing
 557 and plotting the peak power as described above. Selective removal of synapses from PV cells to
 558 the PYR cell yielded an LFP response whose presynaptic origin population was due to the OLM cell

Figure 7. Decomposition of the LFP Signal.

A. All presynaptic cell populations are present. **B.** Only OLM cells are present. **C.** Only BiCs and BC/AACs are present. Schematics on the left show the cell populations projecting to the PYR cell. Computations are done across g_{sb} and g_{bs} parameter values where $c_{sb}=0.21$. For each parameter set, LFPs are computed across all layers and the power spectrum is computed for each layer. The maximum power across all layers is taken as the peak power and given in the color plot. Computation is illustrated to the right of A (see text for details).

Figure 8. Peak Power For All Conductances and Connectivities.

Note that the color scale bars are not the same for all the plots. The plot for $c_{sb}=0.21$ corresponds to Fig 7A.

559 population. The resulting LFP power was low and depended weakly on g_{bs} (Fig 7B). This showed that
 560 OLM cells minimally contributed to the signal power as a presynaptic origin population. Viewing this
 561 from a broader perspective, these results indicated that disinhibition of non-distal apical dendrites
 562 via an indirect (OLM-BiC-PYR) pathway played a much larger role relative to a direct (OLM-PYR)
 563 pathway in producing the LFP power. Along the same lines, disinhibition of distal dendrites through
 564 a BiC-OLM-PYR pathway thus did not have much of an effect on LFP power. Fig 7C shows the result
 565 when we selectively removed the synapses from OLM cells to the PYR cell to yield an LFP response
 566 whose presynaptic origin was the PV cell population. It is clear from the magnitude of the signal
 567 powers in Fig 7C relative to 7B that the theta power was indeed mainly due to the component
 568 from PV cells rather than from OLM cells. Interestingly, the previously seen robustness when all
 569 presynaptic cell populations were present (Fig 7A) was now lost. To quantify all of this, we computed
 570 the mean and standard deviation (std) in units of mV^2/Hz : (5.1×10^{-9} , 1.7×10^{-23}), (9.7×10^{-10} , 5.6×10^{-10}),
 571 (2.6×10^{-8} , 3.8×10^{-8}). When all of the cell populations were present, there was minimal variability,
 572 and when the PV cell populations were removed, the average power decreased five-fold and there
 573 was some variability. However, when only PV cell populations were present, there was an increase
 574 in the average power and the variability was large. It seems clear that OLM cells did not contribute
 575 much to the average LFP power but removing their inputs prominently affected the robustness of
 576 the LFP signal. Therefore, we propose that OLM cells have the capacity to regulate robustness of
 577 LFP responses without affecting the average power.

579 In a recent study, *Amilhon et al. (2015)* showed that SOM cells (putative OLM cells) did not
 580 appear to play a prominent role in the generation of intrinsic LFP theta rhythms since there was
 581 only a weak effect on LFP theta power when they optogenetically silenced SOM cells. Our results
 582 are in agreement with this observation. As shown in Fig 7B, the contribution of OLM cell inputs
 583 to the LFP power was small. To make a more accurate comparison with Amilhon and colleagues'
 584 OLM cell optogenetic silencing experiments we compared the power of the LFP in the predicted
 585 regime in Fig 7A (mean value of $5.1 \times 10^{-9} mV^2/Hz$) with the power of the LFP in Fig 7C for $g_{sb}=0$ and
 586 $g_{bs}=0$ when OLM cell to PYR cell connections were also removed ($8.5 \times 10^{-9} mV^2/Hz$). They were
 587 clearly comparable. It is interesting to note that it was already apparent from Fig 7A that OLM cells
 588 minimally affected LFP power. Consider that for the parameter regime of $g_{sb} = 0$ and across all g_{bs} 's,
 589 the LFP power magnitude was the same ($5.1 \times 10^{-9} mV^2/Hz$) as the average power of the predicted
 590 regime in Fig 7A. In this $g_{sb} = 0$ parameter regime, OLM cell to BiC connections were not present but
 591 the OLM cell to PYR cell connections were still present so that OLM cells could still contribute to the
 592 LFP response via a direct OLM-PYR pathway. Given that the power did not change indicates that any
 593 LFP power contribution due to OLM cells occurred mainly via the indirect OLM-BiC-PYR pathway.
 594 Overall, our results show that OLM cells did participate but in such a way that their presence would
 595 be unnoticed if one were only measuring LFP power.

596 To gain insight into how OLM cells affected the robustness of the LFP signal, we further examined
 597 what was revealed with our LFP decompositions. We observed that with PV or OLM cells removed,
 598 the impaired LFP output could be grouped into certain categories based on their laminar LFP

Figure 9. LFP Pattern Examples In Predicted Regime When Only Either PV Or OLM Cell Populations Are Present.

Peak power color plots as in Fig 7 are shown but with a different color resolution. A gray overlay is added to the plots to emphasize the predicted regime. Three examples of LFP responses (5 sec) across the different layers are shown to illustrate the different patterns observed. For each example, spike rasters for the particular example are shown for PV cells (BiCs and BC/AACs) or OLM cells. **A.** PV cell LFP component. **B.** OLM cell LFP component. Parameter values for left, middle and right columns are respectively: $(g_{sb}, g_{bs}) = (5, 2.75), (5.5, 0.5), (5.75, 1)$ nS.

599 profiles. In Fig 9 we show the peak power plots for the PV cell (Fig 9A) and OLM cell (Fig 9B)
 600 decomposition components in which the non-predicted regime was overlaid with gray. For each
 601 component, we show three examples of the characterized LFP profiles identified in the groupings.
 602 Raster plots that corresponded to each cell population are shown above the examples in the figure.
 603 It is evident that the different LFP patterns cannot be intuited from the raster plots alone. These
 604 examples illustrate the various cases of impaired LFP responses that occurred when OLM or PV cell
 605 connections to the PYR cell were removed.

606 For the middle LFP response examples (low g_{bs} and high g_{sb}) of Fig 9, we note that OLM cells and
 607 BC/AACs had maximal activities and BiCs had minimal activities (see Fig 2C). Thus, synaptic current
 608 influences were obvious at the layers where OLM or BC/AACs contact, and return currents at other
 609 layers. Inappropriate polarity across the layers was manifest. This pattern of impaired LFP response
 610 occurred in about a quarter of the PV cell LFP component parameter sets, and in less than half of
 611 the OLM cell LFP component parameter sets. For the PV cell LFP component, most of the other
 612 parameter sets yielded LFP responses in which there was no rhythm, as shown in the right example
 613 of Fig 9A. Interestingly, in the rest of the cases (less than a third) there was a loss of rhythmicity in
 614 all layers except for the somatic layer as illustrated in the left example. These patterns show that
 615 there was an ongoing 'battle' between basal excitation and PV cell inputs that can yield a wide range
 616 of LFP powers from low (no rhythm - right example) to high (left and middle examples). For the
 617 majority of the OLM cell LFP component parameter sets, there was a loss of rhythmicity as shown
 618 in the left and right examples of Fig 9B. From the temporal profile and polarity, it was clear that the
 619 high amplitude LFP peaks were due to basal excitatory inputs. For larger g_{bs} values, OLM cells were
 620 less active (see Fig 2C) and LFP responses across the layers became dominated by peaks due to
 621 basal excitation rather than synaptic and return currents due to OLM cells. Overall, cancellations
 622 and rhythm loss occurred due to interactions between OLM cells' synaptic and return currents and
 623 excitatory inputs. As summarized in the peak power plots of Fig 7C or Fig 9A, PV cell inputs alone
 624 were not capable of sustaining the robustness throughout the predicted regime and the impaired
 625 LFP signals showed a large variability. With OLM cell inputs alone, there was low LFP power either
 626 because of loss of rhythmicity or because of low amplitude rhythms (Fig 7B or Fig 9B peak power
 627 plots).

628 **With and without basal excitation**

629 As one might expect, including basal excitation to incoming inhibitory inputs from different cell
 630 populations added to the complexity of untangling nonlinear, interacting components producing
 631 the LFP. We relied on our developed intuition when basal excitation was not included (Fig 2A,B) and
 632 our LFP decompositions to help reveal the different roles that OLM cells and PV cells might play in
 633 LFP theta rhythms. Specifically, we can understand that the loss of LFP rhythm at some layers likely
 634 occurred because of having a 'balance' of synaptic and return currents for various conductance
 635 values leading to LFP rhythm cancellation or an inappropriate negative polarity domination (see Fig
 636 2A(iii) and B(iii)). Thus, in finding that the LFP power was a robust feature in the predicted regime of
 637 synaptic conductance and connection probabilities, we were able to understand that it was critically
 638 the OLM cell population that brought about this robust feature. However, this robust feature was
 639 apparent only when basal excitation was included. This is clearly visualized in Fig 10 where we
 640 plot the peak power color plots with and without basal excitation when all cells were present or

Figure 10. Peak Power Plots With and Without Basal Excitation.

The color plots represent peak power as described in Fig 7 and with a gray overlay as in Fig 9. Note that different color resolutions are used here to facilitate comparison for particular cell populations (i.e., any row). With and without basal excitation is shown on the left and right columns respectively. **Top:** All cell populations. **Middle:** OLM cell LFP component. **Bottom:** PV cell LFP component.

641 with only OLM cell or PV cell LFP components. Removal of basal excitatory inputs in the case when
 642 all cells were present (Fig 10, top) led to a loss of robustness. The mean and std in the predicted
 643 regime without basal excitation was $6.2 \times 10^{-9} \text{ mV}^2/\text{Hz}$ and $8.0 \times 10^{-9} \text{ mV}^2/\text{Hz}$ respectively. While
 644 the mean was comparable to when basal excitation was present, the standard deviation was much
 645 larger (see values with basal excitation above). Co-activation of inhibition and excitation was clearly
 646 important for this robust feature to emerge.

647 From the LFP decompositions and different LFP patterns expressed (see Fig 7B), and OLM cell
 648 activities (see Fig 2C), we can understand that the contribution of OLM cells was more dependent
 649 on g_{bs} than g_{sb} with the basal excitation affecting the peak power robustness more for larger g_{bs}
 650 values. This was apparent in the color variation of the plots of the OLM cell LFP component in Fig 10
 651 (middle). It was larger with basal excitation (left) than without basal excitation (right) for larger g_{bs}
 652 values. This was reflected in the mean and standard deviation without basal excitation (5.2×10^{-10}
 653 mV^2/Hz , $2.2 \times 10^{-10} \text{ mV}^2/\text{Hz}$) that was smaller than with basal excitation (see values with basal
 654 excitation above). With only the PV cell LFP component, the LFP theta rhythm was disrupted as the
 655 interactions between basal excitation and PV inhibitory inputs were missing the OLM cell inputs.
 656 Specifically, the mean and std without basal excitation was ($8.0 \times 10^{-9} \text{ mV}^2/\text{Hz}$, $1.1 \times 10^{-8} \text{ mV}^2/\text{Hz}$)
 657 which was smaller than with basal excitation (see values with basal excitation above). In essence,
 658 the inclusion of basal excitation can be considered as 'adding' to the magnitude and variance of
 659 the LFP power when OLM cells or PV cells were examined separately. In combination, a synergistic
 660 effect between inhibition and excitation occurred to generate a robust regime - a mean power with
 661 minimal variance. From Fig 2C, it can be seen that the PV cells (BC/AACs and BiCs) had activities
 662 that were more dependent on g_{sb} than on g_{bs} , and that BC/AACs were relatively more active than
 663 BiCs in the predicted regime. Thus, at larger g_{bs} values when OLM cells were less active, BC/AACs
 664 would contribute more to keeping a synergistic balance with the basal excitation.

665 LFP power across layers

666 As illustrated in Fig 7A, the color peak power plots are the power in the layer (particular electrode)
 667 where the power was maximal. To fully express this, we plotted the maximum LFP power across
 668 the dendritic tree for all parameter sets in the predicted regime. This is shown in Fig 11A with
 669 insets showing the same for the OLM cell (top) and PV cell (bottom) LFP components. From this,
 670 we see that the maximum LFP power was recorded at electrode 4, and that with only the OLM
 671 cell component, the power was distributed more widely and with only the PV cell component,
 672 more narrowly focused around the soma. This thus shows that the two populations differentially
 673 influenced the location of LFP maxima. That the LFP power showed no discernible variability when
 674 all the cell populations were present, and that there was clear variability when not all of the cell
 675 populations were present is obvious in this Fig 11A. We did several additional sets of simulations to
 676 explore whether changes in the synaptic weights on the PYR cell would affect whether the robust
 677 power feature in the predicted regime would still be present. In all the simulations presented so
 678 far, we used synaptic weights that did not bias the effect of one cell population type over the other
 679 based on their synaptic input location. So, for example, OLM cell inputs that were the furthest away
 680 from the soma had the largest synaptic weight. In doing this, we were following what was done
 681 previously in *Ferguson et al. (2015)* who used 'unbiased' synaptic weights as well as using the same
 682 synaptic weight for all of the cell types. In using the same synaptic weight for all the cell types, we
 683 found that the robust power feature in the predicted regime remained (not shown).

684 As described and shown above, it was already clear that OLM cells via a direct OLM-PYR pathway

Figure 11. Laminar Power and Peak Power Changes With Changing Synaptic Weights.

A. Computed power at the different electrode locations to show laminar power distribution, for all sets of parameter values in the predicted regime. Top inset: Laminar power for OLM cell LFP component. Bottom inset: Laminar power for PV cell LFP component. Schematics shows the PYR cell model with the 15 extracellular electrodes and the different network configurations. **B.** Changing the synaptic weight from the OLM cells to the PYR cell does not lead to much change in the peak power, as illustrated by the peak power at electrode 4. Parameter values: $g_{sb} = 5.25$, $g_{bs} = 5.00$ nS. Synaptic weights of 0.00067, 0.001, 0.002, 0.003, 0.004 μ S are shown.

Figure 12. Spatial Attenuation.

We estimated the spatial extent of the generated LFP using our models. PYR cell model morphology is shown with calculated signal decrease from a electrode positioned near the cell soma. The dotted arrow shows the extent of the spatial reach of the signal that is taken as a 99% decrease in the signal, and is approximately 300 μ m. Parameter values used are from the predicted regime. $g_{sb}=5$, $g_{bs}=5.75$ nS, $c_{sb}=0.21$.

685 minimally contributed to the LFP theta power. To show this directly, we did several, additional
686 simulations where we changed the synaptic weight from OLM cells to the PYR cell. As an example,
687 in Fig 11B we show that increasing the synaptic weight by almost an order of magnitude decreased
688 the peak power by only about 20%.

Estimating the number of PYR cells that contribute to the LFP signal

689 It is challenging to know how many cells contribute to an extracellular recording. The hippocampus
690 has a regular cytoarchitecture with a nearly laminar, stratified structure of pyramidal cells (*Andersen*
691 *et al.*, 2006). This arrangement together with pyramidal cells being of similar morphologies and
692 synaptic input profiles means that we can assume that any given pyramidal cell will generate
693 a similar electric field leading to an additive effect in the extracellular space with multiple cells
694 in resulting LFP dipole recordings. Further, for the *in vitro* intrinsic theta LFP generation being
695 considered in this work, the focus can be justified to the couple of synaptic pathways that we
696 explored, and incoming inputs were synchronized amplifying the additive effect.

698 To estimate how many PYR cells contributed to an extracellular LFP recording in the *in vitro*
699 whole hippocampus preparation, we defined the ‘spatial reach’ of the LFP as the radius around the
700 electrode where the LFP amplitude was decreased by 99%. Using our biophysical computational
701 LFP models with parameter values taken from the predicted regime, we found that the spatial
702 reach is 300 μ m as measured extracellularly close to the soma since the LFP decreased from 10,000
703 nV to 100 nV within this radius. This is shown in Fig 12 where the dotted arrow represents this
704 radius. Therefore, from a “neuron-centric” approach the LFP declined to 1% of its original power
705 within 300 μ m. From an “electrode-centric” point of view this means that if we were to place an
706 electrode extracellularly to the soma of a given neuron then that electrode would pick up signal
707 from neurons within 300 μ m as any neuron 300 μ m further away would contribute to the recorded
708 signal by less than 1% of its maximum power. To estimate the number of cells present within this
709 spatial extent we turned to literature. Taking advantage of detailed quantitative assessment and
710 modeling done by Bezaire and colleagues (*Bezaire and Soltesz, 2013; Bezaire et al., 2016*), there are
711 about 311,500 PYR cells in a volume of 0.2 mm³ of ‘stratum pyramidale’ tissue (see model specifics
712 in Fig 1 of *Bezaire et al. (2016)*). Given our spatial reach radius estimate, a cylindrical volume of
713 stratum pyramidale would be 0.014 mm³ or about 7% of the total number of PYR cells which is
714 about 22,000. In this way we estimated that there would be about 22,000 PYR cells that contributed
715 to the LFP signal. We note that this would be an upper bound, as we assumed correlated activity
716 across pyramidal cells and homogeneous extracellular electrical properties.

Discussion

718 To a large extent, understanding brain function and coding requires that we are able to understand
719 how oscillatory LFP signals are generated (*Einevoll et al., 2013; Friston et al., 2015; Hyafil et al.,*

720 **2015**). Cross-frequency coupling analyses of LFP signals has led to ideas underlying learning
721 and memory functioning (*Canolty and Knight, 2010*), and it is always important to do careful
722 analyses (*Scheffer-Teixeira and Tort, 2016*). Further, given that particular inhibitory cell populations
723 and abnormalities in theta rhythms are associated with disease states (*Colgin, 2016*), we need
724 to consider how different cell types and pathways contribute to LFP recordings. Ultimately, the
725 challenge is to bring together LFP studies from experimental, modeling and analysis perspectives.
726 In this work, we make steps toward this challenge by gaining insight into the contribution of OLM
727 cells to *intrinsic* theta rhythms as exhibited by an *in vitro* whole hippocampus preparation.

728 **Theta rhythms and summary of results**

729 The existence of theta rhythms (3-12 Hz) in the hippocampus has long been known, and these
730 prevalent rhythms are associated with memory processing and spatial navigation (*Colgin, 2013,*
731 *2016*). These rhythms are present when the animal is actively exploring and during REM sleep.
732 Further, they can be separated into higher or lower frequencies that are atropine-resistant or
733 atropine-sensitive respectively (*Buzsáki, 2002; Colgin, 2013, 2016*). Recent work has shown that low
734 theta rhythms were elicited in rats with fearful stimuli and high theta with social stimuli (*Tendler*
735 *and Wagner, 2015*). *In vitro* models of theta rhythms in the hippocampus have been developed (e.g.,
736 *Gillies et al. (2002)*) as well as network mathematical models (e.g., *Neymotin et al. (2011); Hummos*
737 *and Nair (2017)*), but it is challenging to bring about a mechanistic understanding of theta rhythms
738 *in vivo* due to their various forms and pharmacological sensitivities combined with the interactions
739 that occur between the hippocampus and other brain structures.

740 While it is clear that different interneuron subtypes are involved in theta rhythms (*Colgin, 2013,*
741 *2016*), it is difficult to untangle the cellular contributions to resulting theta rhythms exhibited
742 in extracellular LFP recordings. That the required circuitry for theta rhythms has been shown
743 to be present in local circuits of the hippocampus (*Colgin and Moser, 2009*) is both useful and
744 helpful as it becomes more likely that biophysical LFP models can be linked to a cellular-based
745 circuit understanding of theta rhythms. We took advantage of the *in vitro* whole hippocampus
746 preparation that spontaneously expressed *intrinsic* theta rhythms (*Goutagny et al., 2009*), and
747 previous inhibitory network models developed for this experimental context (*Ferguson et al., 2015*),
748 to build biophysical LFP models.

749 The LFP is generated on the basis of transmembrane currents. This means that the LFP is a
750 weighted sum of inward and outward currents. How the LFP changes as a function of location is not
751 trivial. In our work here, when the LFP is governed by synaptic inputs the LFP peaks are narrower
752 since the synaptic inputs are synchronized because of the coherent inhibitory spike rasters. On the
753 other hand LFP signals governed by return currents would produce LFP peaks that are less narrow as
754 the signal slows down as it travels down the dendrites producing a time lag. This all thus translates
755 to synaptic input location dependencies. Thus, while we can visualize and appreciate the synergistic
756 balances between excitation and inhibition from different cell populations, we note that these
757 combinations are not easily seen as summated balances. Signal decompositions and intuitions
758 from many simulations are required. We leveraged our LFP models to make direct comparison with
759 experimental LFP characteristics. This allowed us to constrain coupling parameters which in turn
760 led us to understand the cellular contribution of interneuron subtypes, specifically OLM cells, to
761 *intrinsic* theta LFP rhythms.

762 We showed how the extracellular theta field recorded along the cellular axis of a PYR cell
763 was affected by the magnitude of the inhibitory synaptic currents inserted along its dendritic
764 arbor. Fluctuations in the magnitude of the total inhibitory input occurred due to alterations in
765 synaptic strength balances of the inhibitory networks. Our models exhibited network states in
766 which interactions between OLM cells and BiCs could invert the polarity of the recorded signal and
767 produce extracellular potentials of high or low magnitude. We also distinguished regimes where
768 these cellular interactions preserved the frequency of the signal versus those that led to lags or
769 abolishments of the extracellular LFP rhythm. When we applied experimental characteristics of

770 theta frequencies and polarities to our biophysical LFP models, a clear selection emerged and thus
771 we were able to constrain parameter values regarding connectivities. Specifically, we found that the
772 connection probability from OLM cells to BiCs needed to be 0.21 and that synaptic conductances
773 from OLM cells to BiCs had to be larger than 3.5 nS, and we called this the *predicted regime*.

774 Unexpectedly, we found that this predicted regime also exhibited a robust power output. That
775 is, so long as parameter values were within the predicted regime, the power did not change (Fig 7A),
776 and in this regime we saw that BiCs were mostly silenced, BC/ACCs were significantly active while
777 OLM cell activity decreased from high to low values as g_{hs} increased (Fig 2C). By decomposing the
778 signal we revealed that OLM cell inputs minimally contributed to the LFP power unlike the other
779 cell populations (BiCs and BC/AACs or PV cells). The power of the OLM cell LFP component on
780 its own, although low, showed some variation in the predicted regime (coefficient of variation or
781 CV < 1). On the other hand, the power of the PV cell LFP component was a couple of orders of
782 magnitude higher and showed more variation (CV > 1) in the predicted regime. This indicates that
783 OLM cells contributed to LFP power robustness without contributing to average power whereas PV
784 cells contributed to average power but their effect was more sensitive to perturbations in OLM-BiC
785 interactions. Therefore their contribution was variable. It is however interesting to note that the PV
786 LFP component average power was larger than the average power of the predicted regime with
787 all cells being present. Thus our results indicated that adding OLM cells in the network can overall
788 cause a small decrease in LFP average power as compared to when only PV cells were present and
789 of course induce robustness. It was also interesting to observe that in almost half of the cases the
790 OLM cell LFP component was arrhythmic or non-oscillatory despite the fact that OLM cells were
791 driven by theta-paced EPSCs. That is, OLM cell inputs alone in most cases were not able to generate
792 a theta LFP signal as recorded in the extracellular space of the PYR cell even though OLM cell
793 populations themselves were firing at theta frequency. Further LFP signal analysis decomposition
794 showed that removing only basal excitation disrupted the robustness of the predicted regime. This
795 suggests that a synergy of OLM cell inputs and basal excitatory inputs as co-activation of distal
796 inhibition and proximal excitation is important to produce robustness in the predicted regime.
797 Overall, an essential aspect in comparing model and experiment LFPs to predict model parameters
798 and decipher cellular contributions was to match sources and sinks at different layers. Thus, having
799 recordings from multiple layers is important.

800 **Morphological details, synaptic locations and related studies**

801 As the main contribution to the LFP is thought to stem from synaptic input to neurons and the sub-
802 threshold dendritic processing, various studies have investigated how morphological characteristics
803 and intrinsic resonances shape the features of the LFP signal. In most cases input synapses are
804 activated according to Poissonian statistics (Łęski *et al.*, 2013; Lindén *et al.*, 2010; Ness *et al.*, 2016).
805 However, in our study here the origin population consisted of point neuron cell representations that
806 had been constrained based on experimental patch clamp recordings from the whole hippocampus
807 preparation. We used a scheme which is a combination of point neuron origin populations and a
808 multi-compartment PYR cell model which served as a processor of synaptic inputs and produced
809 the LFP. This scheme is conceptually very similar to the hybrid scheme proposed in (Hagen *et al.*,
810 2016).

811 One factor modulating the amplitude of LFPs was related to the somatodendritic location
812 of synaptic inputs on the PYR cell tree. Different populations of GABAergic interneurons target
813 different dendritic domains and the domain-specific targeting of various interneurons supports
814 the hypothesis of domain-specific synaptic integration in CA1 PYR cells (Spruston, 2008). In CA1
815 PYR cells, distal and middle apical dendrites comprise two distinct dendritic domains with separate
816 branching connected by a thick apical dendrite. This cytoarchitectonic separation of the cluster
817 of distal dendrites relative to middle and proximal dendrites was shown to critically reduce the
818 effect of distal EPSCs to somatic excitability (Srinivas *et al.*, 2017). The presence of a single apical
819 dendrite with many obliques in stratum radiatum caused a large shunting of EPSCs traveling from

820 the tuft dendrites to the soma. Thus we can appreciate our observation that OLM cells, which target
821 distal dendrites, minimally affected LFP power in stratum pyramidale considering the limited ability
822 of distal inhibition to reach more proximal and somatic regions of the CA1 PYR where maximum
823 power was recorded. This is not just due to the distal location of these inputs but more due to
824 the cytoarchitectonic separation of the cluster of distal dendrites relative to middle and proximal
825 dendrites. This separation prohibited inhibitory inputs in distal regions from effectively propagating
826 to somatic and proximal regions of CA1 PYR cells and thus being reflected in the extracellular space.

827 We can further consider our results in light of another theoretical modeling study by *Gidon and*
828 *Segev (2012)* which showed that inhibitory inputs can affect excitatory inputs locally and/or globally,
829 depending on the relative locations of the excitatory and inhibitory synapses. In particular this
830 can help us understand the loss of robust power in the predicted regime after removal of OLM
831 cells. The predicted regime consists of different connectivities that generated different spiking
832 patterns that gave rise to fluctuations in inhibitory input in different synaptic locations. First,
833 inhibitory input hyperpolarized the membrane potential, which resulted in shunting of the adjacent
834 dendritic compartments. Activation of excitatory synapses within the shunted compartments will
835 thus generate smaller depolarization, compared with non-shunted dendrites (“local” effect). Second,
836 the local shunting would suppress excitatory input in a nonlinear fashion at locations that were
837 not directly affected by the shunting (“global” effect). Thus, when inhibitory inputs were activated
838 simultaneously with excitatory inputs, the average (i.e., across trials) evoked membrane potential
839 within shunted dendritic compartments should be smaller compared with compartments that
840 had no inhibitory input. At the same time, excitatory effects throughout the entire dendritic tree
841 would be reduced in a nonlinear fashion, and which can be quantified as the change (with versus
842 without inhibitory input) of the trial-to-trial variability of the membrane potential. In our case the
843 activation of excitatory inputs occurred in regions not close by the OLM cell inhibitory inputs, thus
844 the overall power did not increase but the robustness was affected. In *Gidon and Segev (2012)* the
845 authors examined the spread of shunt level implications using a CA1 reconstructed neuron model
846 receiving inhibition at three distinct dendritic subdomains: the basal, the apical, and the oblique
847 dendrites as innervated by inhibitory synapses. They found that the shunt level spread effectively
848 hundreds of micrometers centripetally to the contact sites themselves spanning from the distal
849 dendrites to the somatic area. This observation thus showed that the somatic area was indeed
850 influenced by shunting inhibition which means that excitatory input non-linearities in our model
851 will be reduced in the presence of global inhibition in the somatic area leading to a decrease in
852 variability and thus robustness in the membrane potential. Of course, the LFP is a measurement of
853 transmembrane currents and not membrane potential. However the reduction of excitatory input
854 mediated non-linearities will also reduce the variability in the distribution of return currents and
855 thus the variability in the LFP.

856 **Limitations and future considerations**

857 Our present study was limited in terms of not considering more inhibitory cell types (e.g., see *Bezaire*
858 *et al. (2016)*) and by considering *ongoing* intrinsic theta rhythms since theta frequency inputs were
859 used (Fig 1). However, our inhibitory network models were constrained by the experimental context
860 and our less complex model representations enabled us to explore many thousands of simulations
861 and directly compare our biophysical LFPs with experimental LFP features. This aspect was key in
862 allowing us to constrain parameter value sets and to gain insights.

863 Theta rhythms are foremost generated due to subthreshold activity and dendritic processing
864 of synaptic inputs. Here we used a passive PYR cell model as the spiking component has been
865 shown to mainly contribute to the LFP at frequencies higher than 90Hz (*Schomburg et al., 2012*)
866 while the active voltage-gated channels that were eliminated here were shown to influence LFP
867 characteristics more prominently in frequencies above the theta range (*Reimann et al., 2013*).
868 Thus, although the presence of voltage-gated channels will influence the exact distribution of
869 return currents, we thought that it was a reasonable simplification to not include them in this

870 study. Indeed in an additional set of simulation (data not shown) we observed that the presence
871 of hyperpolarization-activated cyclic nucleotide-gated (HCN) channels on the pyramidal cell did
872 not influence the sink-source LFP profile and frequency examined here although it did affect the
873 waveform characteristics.

874 Another limitation is the usage of a single pyramidal cell to predict network dynamics. However
875 we note here that since the LFP is a linear summation of the transmembrane currents in the
876 extracellular space (Equation 1), incorporating more PYR cells could result in a linear additive effect
877 in the extracellular space. This would lead to the same LFP profiles as in the case of a single cell only
878 significantly magnified provided that the cells have a similar morphology, physically arborizing in
879 ways that facilitate superposition rather than cancellations of fields, and receive similar presynaptic
880 inputs. Indeed, there is a homogeneous cytoarchitecture disposition of the pyramidal cells across
881 the CA1 layer (*Andersen et al., 2006*) and is one of the factors responsible for the extracellular
882 sinks and sources recorded in CA1. Also, pyramidal cells receive similar presynaptic inputs from the
883 presynaptic populations which project upon the same layers across cells. For this reason we do
884 think that the conclusions derived from the single cell LFP output will remain on the network level
885 to some extent. Of course, important variabilities across pyramidal cells also exist and considering
886 them in future studies will be important (e.g., see (*Soltesz and Losonczy, 2018*)). Therefore careful
887 network modelling will be required to assess the network-generated LFP output.

888 Extracellular studies suggest that the main current generators of field theta waves are the
889 coherent dendritic and somatic membrane potential fluctuations of the orderly aligned pyramidal
890 cells (*Winson, 1978; Buzsáki and Eidelberg, 1983; Brankačk et al., 1993*). Thus, distal and local
891 ascending pathways onto PYR cells can in principle contribute to extracellular LFP deflections. To
892 understand theta rhythms one needs to consider the populations projecting onto the PYR cells in
893 CA1. During *in vivo* behaviors, medial septum and entorhinal cortical inputs onto CA1 PYR cells
894 are prominent modulators of the amplitude, phase and waveform features of theta rhythms in
895 conjunction with local inhibitory and excitatory cells. However, spatiotemporal coincidence of
896 inputs makes separation difficult and thus it is challenging to determine cellular contributions
897 to LFP recordings. As there is significant spatiotemporal overlap on PYR cell dendrites across
898 ascending pathways it would be hard to disentangle the cellular composition of these pathways
899 and assess the cellular contribution to theta LFP characteristics. As shown in previous studies
900 (*Makarova et al., 2011*) blind separation techniques such as Independent Component Analysis
901 produce poor results when trying to disentangle combinations of rhythmic synaptic sources with
902 extensive spatiotemporal overlap. By focusing on intrinsic theta rhythms in the *in vitro* whole
903 hippocampus preparation here, we reduced the spatiotemporal overlap of different pathways
904 and unravelled the cellular composition of the different pathways projecting to the PYR cell. We
905 were thus able to decipher the contribution of OLM cells to intrinsic theta rhythms. This work
906 could potentially be used as a basis to understand OLM cell contributions during *in vivo* theta LFP
907 recordings.

908 Moving forward we aim to take advantage of the insights gained here to build hypothesis-driven
909 theta generating networks. In this way, we hope to be able to determine the contribution of
910 different cell types and pathways to LFP recordings that are so heavily used and interpreted in
911 neuroscience today.

912 References

- 913 **Amihon B**, Huh CYL, Manseau F, Ducharme G, Nichol H, Adamantidis A, et al. Parvalbumin Interneurons
914 of Hippocampus Tune Population Activity at Theta Frequency. *Neuron*. 2015 Jun; 86(5):1277–1289. doi:
915 [10.1016/j.neuron.2015.05.027](https://doi.org/10.1016/j.neuron.2015.05.027).
- 916 **Andersen P**, Morris R, Amaral D, Bliss T, O'Keefe J. *The Hippocampus Book*. 1 ed. Oxford University Press, USA;
917 2006.
- 918 **Baude A**, Bleasdale C, Dalezios Y, Somogyi P, Klausberger T. Immunoreactivity for the GABAA Receptor $\alpha 1$

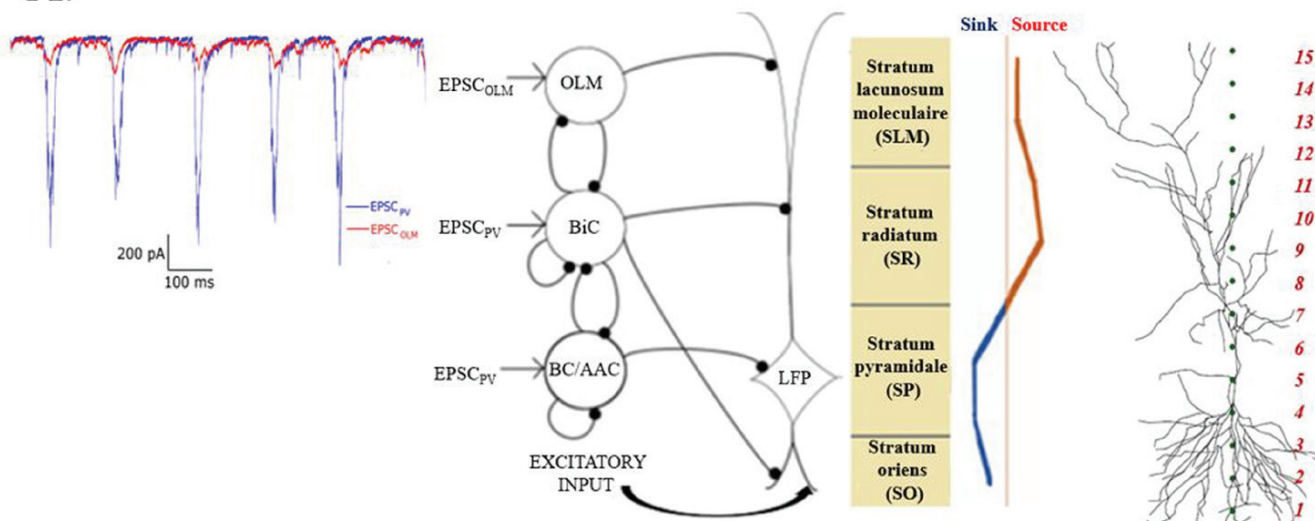
- 919 Subunit, Somatostatin and Connexin36 Distinguishes Axoaxonic, Basket, and Bistratified Interneurons of the
920 Rat Hippocampus. *Cerebral Cortex*. 2007 Sep; 17(9):2094–2107. doi: 10.1093/cercor/bhl117.
- 921 **Bezaire MJ**, Raikov I, Burk K, Vyas D, Soltesz I. Interneuronal mechanisms of hippocampal theta oscillation in a
922 full-scale model of the rodent CA1 circuit. *eLife*. 2016 Dec; 5:e18566. doi: 10.7554/eLife.18566.
- 923 **Bezaire MJ**, Soltesz I. Quantitative assessment of CA1 local circuits: Knowledge base for interneuron-pyramidal
924 cell connectivity. *Hippocampus*. 2013 May; doi: 10.1002/hipo.22141.
- 925 **Brankačk J**, Stewart M, E Fox S. Current source density analysis of the hippocampal theta rhythm: associated
926 sustained potentials and candidate synaptic generators. *Brain Research*. 1993 Jul; 615(2):310–327. <http://www.sciencedirect.com/science/article/pii/000689939390043M>, doi: 10.1016/0006-8993(93)90043-M.
- 927
928 **Buzsáki G**, Eidelberg E. Phase relations of hippocampal projection cells and interneurons to theta activity in the
929 anesthetized rat. *Brain Research*. 1983 May; 266(2):334–339. <http://www.sciencedirect.com/science/article/pii/0006899383906650>, doi: 10.1016/0006-8993(83)90665-0.
- 930
931 **Buzsáki G**. Theta oscillations in the hippocampus. *Neuron*. 2002 Jan; 33(3):325–340.
- 932 **Buzsáki G**. *Rhythms of the Brain*. 1 ed. Oxford University Press, USA; 2006.
- 933 **Buzsáki G**, Anastassiou CA, Koch C. The origin of extracellular fields and currents — EEG, ECoG, LFP and spikes.
934 *Nature Reviews Neuroscience*. 2012 Jun; 13(6):407–420. <http://www.nature.com/myaccess.library.utoronto.ca/nrn/journal/v13/n6/full/nrn3241.html>, doi: 10.1038/nrn3241.
- 935
936 **Buzsáki G**, Draguhn A. Neuronal Oscillations in Cortical Networks. *Science*. 2004 Jun; 304(5679):1926–1929.
937 <http://www.sciencemag.org/content/304/5679/1926.abstract>, doi: 10.1126/science.1099745.
- 938 **Canolty RT**, Knight RT. The functional role of cross-frequency coupling. *Trends in Cognitive Sciences*.
939 2010 Nov; 14(11):506–515. <http://www.sciencedirect.com/science/article/pii/S1364661310002068>, doi:
940 10.1016/j.tics.2010.09.001.
- 941 **Carmichael JE**, Gmaz JM, van der Meer MAA. Gamma Oscillations in the Rat Ventral Striatum Originate in the
942 Piriform Cortex. *Journal of Neuroscience*. 2017 Aug; 37(33):7962–7974. <http://www.jneurosci.org/content/37/33/7962>, doi: 10.1523/JNEUROSCI.2944-15.2017.
- 943
944 **Carnevale NT**, Hines ML. *The NEURON Book*. Cambridge: Cambridge University Press; 2006. <http://ebooks.cambridge.org/ref/id/CBO9780511541612>.
- 945
946 **Colgin LL**. Mechanisms and Functions of Theta Rhythms. *Annual Review of Neuroscience*. 2013; 36(1):295–312.
947 doi: 10.1146/annurev-neuro-062012-170330.
- 948 **Colgin LL**. Rhythms of the hippocampal network. *Nature Reviews Neuroscience*. 2016 Apr; 17(4):239–249. doi:
949 10.1038/nrn.2016.21.
- 950 **Colgin LL**, Moser EI. Hippocampal theta rhythms follow the beat of their own drum. *Nature Neuroscience*. 2009
951 Dec; 12(12):1483–1484. doi: 10.1038/nn1209-1483.
- 952 **Einevoll GT**, Kayser C, Logothetis NK, Panzeri S. Modelling and analysis of local field potentials for studying the
953 function of cortical circuits. *Nature Reviews Neuroscience*. 2013 Nov; 14(11):770–785. doi: 10.1038/nrn3599.
- 954 **Ferguson KA**, Chatzikalymniou AP, Skinner FK. Combining Theory, Model, and Experiment to Explain How
955 Intrinsic Theta Rhythms Are Generated in an In Vitro Whole Hippocampus Preparation without Oscillatory
956 Inputs. *eNeuro*. 2017 Aug; 4(4). doi: 10.1523/ENEURO.0131-17.2017.
- 957 **Ferguson KA**, Huh CYL, Amilhon B, Manseau F, Williams S, Skinner FK. Network models provide insights into
958 how oriens-lacunosum-moleculare and bistratified cell interactions influence the power of local hippocampal
959 CA1 theta oscillations. *Frontiers in Systems Neuroscience*. 2015; 9:110. doi: 10.3389/fnsys.2015.00110.
- 960 **Ferguson KA**, Huh CYL, Amilhon B, Williams S, Skinner FK. Experimentally constrained CA1 fast-firing
961 parvalbumin-positive interneuron network models exhibit sharp transitions into coherent high frequency
962 rhythms. *Frontiers in Computational Neuroscience*. 2013; 7:144. doi: 10.3389/fncom.2013.00144.
- 963 **Friston KJ**, Bastos AM, Pinotsis D, Litvak V. LFP and oscillations—what do they tell us? *Current Opinion in
964 Neurobiology*. 2015 Apr; 31:1–6. <http://www.sciencedirect.com/science/article/pii/S0959438814001056>, doi:
965 10.1016/j.conb.2014.05.004.

- 966 **Gidon A**, Segev I. Principles Governing the Operation of Synaptic Inhibition in Dendrites. *Neuron*. 2012 Jul; 75(2):330–341. [http://www.cell.com/neuron/abstract/S0896-6273\(12\)00481-3](http://www.cell.com/neuron/abstract/S0896-6273(12)00481-3), doi: 10.1016/j.neuron.2012.05.015.
- 967
968
- 969 **Gillies MJ**, Traub RD, LeBeau FEN, Davies CH, Gloveli T, Buhl EH, et al. A Model of Atropine-Resistant Theta Oscillations in Rat Hippocampal Area CA1. *The Journal of Physiology*. 2002 Sep; 543(3):779–793. doi: 10.1113/jphysiol.2002.024588.
- 970
971
- 972 **Goutagny R**, Jackson J, Williams S. Self-generated theta oscillations in the hippocampus. *Nature Neuroscience*. 2009 Dec; 12(12):1491–1493. doi: 10.1038/nn.2440.
- 973
- 974 **Hagen E**, Dahmen D, Stavrinou ML, Lindén H, Tetzlaff T, van Albada SJ, et al. Hybrid Scheme for Modeling Local Field Potentials from Point-Neuron Networks. *Cerebral Cortex (New York, NY: 1991)*. 2016 Dec; 26(12):4461–4496. doi: 10.1093/cercor/bhw237.
- 975
976
- 977 **Hattori R**, Kuchibhotla KV, Froemke RC, Komiyama T. Functions and dysfunctions of neocortical inhibitory neuron subtypes. *Nature Neuroscience*. 2017 Sep; 20(9):1199–1208. doi: 10.1038/nn.4619.
- 978
- 979 **Herreras O**. Local Field Potentials: Myths and Misunderstandings. *Frontiers in Neural Circuits*. 2016; 10. doi: 10.3389/fncir.2016.00101.
- 980
- 981 **Huh CYL**, Amilhon B, Ferguson KA, Manseau F, Torres-Platas SG, Peach JP, et al. Excitatory Inputs Determine Phase-Locking Strength and Spike-Timing of CA1 Stratum Oriens/Alveus Parvalbumin and Somatostatin Interneurons during Intrinsically Generated Hippocampal Theta Rhythm. *The Journal of Neuroscience*. 2016 Jun; 36(25):6605–6622. doi: 10.1523/JNEUROSCI.3951-13.2016.
- 982
983
984
- 985 **Hummos A**, Nair SS. An integrative model of the intrinsic hippocampal theta rhythm. *PLOS ONE*. 2017 Aug; 12(8):e0182648. doi: 10.1371/journal.pone.0182648.
- 986
- 987 **Hyafil A**, Giraud AL, Fontolan L, Gutkin B. Neural Cross-Frequency Coupling: Connecting Architectures, Mechanisms, and Functions. *Trends in Neurosciences*. 2015 Nov; 38(11):725–740. <http://www.sciencedirect.com/science/article/pii/S0166223615002088>, doi: 10.1016/j.tins.2015.09.001.
- 988
989
- 990 **Izhikevich EM**. Simple model of spiking neurons. *IEEE Transactions on Neural Networks*. 2003 Nov; 14(6):1569–1572. doi: 10.1109/TNN.2003.820440.
- 991
- 992 **Kepecs A**, Fishell G. Interneuron cell types are fit to function. *Nature*. 2014 Jan; 505(7483):318–326. http://www.nature.com.myaccess.library.utoronto.ca/nature/journal/v505/n7483/full/nature12983.html?WT.ec_id=NATURE-20140116#outlook, doi: 10.1038/nature12983.
- 993
994
- 995 **Klausberger T**, Somogyi P. Neuronal Diversity and Temporal Dynamics: The Unity of Hippocampal Circuit Operations. *Science*. 2008 Jul; 321(5885):53–57. <http://www.sciencemag.org/content/321/5885/53.abstract>, doi: 10.1126/science.1149381.
- 996
997
- 998 **Leão RN**, Mikulovic S, Leão KE, Munguba H, Gezelius H, Enjin A, et al. OLM interneurons differentially modulate CA3 and entorhinal inputs to hippocampal CA1 neurons. *Nature Neuroscience*. 2012; 15(11):1524–1530. doi: 10.1038/nn.3235.
- 999
1000
- 1001 **Lindén H**, Hagen E, Leski S, Norheim ES, Pettersen KH, Einevoll GT. LFPy: a tool for biophysical simulation of extracellular potentials generated by detailed model neurons. *Frontiers in Neuroinformatics*. 2014; 7:41. doi: 10.3389/fninf.2013.00041.
- 1002
1003
- 1004 **Lindén H**, Pettersen KH, Einevoll GT. Intrinsic dendritic filtering gives low-pass power field potentials. *Journal of Computational Neuroscience*. 2010 Dec; 29(3):423–444. doi: 10.1007/s10827-010-0245-4.
- 1005
- 1006 **Loken C**, Gruner D, Groer L, Peltier R, Bunn N, Craig M, et al. SciNet: Lessons learned from building a power-efficient top-20 system and data centre. *Journal of Physics: Conference Series*. 2010; 256:012026.
- 1007
- 1008 **López-Aguado L**, Ibarz JM, Herreras O. Activity-dependent changes of tissue resistivity in the CA1 region in vivo are layer-specific: modulation of evoked potentials. *Neuroscience*. 2001 Dec; 108(2):249–262. doi: 10.1016/S0306-4522(01)00417-1.
- 1009
1010
- 1011 **Maccaferri G**. Stratum oriens horizontal interneurone diversity and hippocampal network dynamics. *The Journal of Physiology*. 2005 Jan; 562(Pt 1):73–80. <http://www.ncbi.nlm.nih.gov/pubmed/15498801>, doi: 10.1113/jphysiol.2004.077081.
- 1012
1013

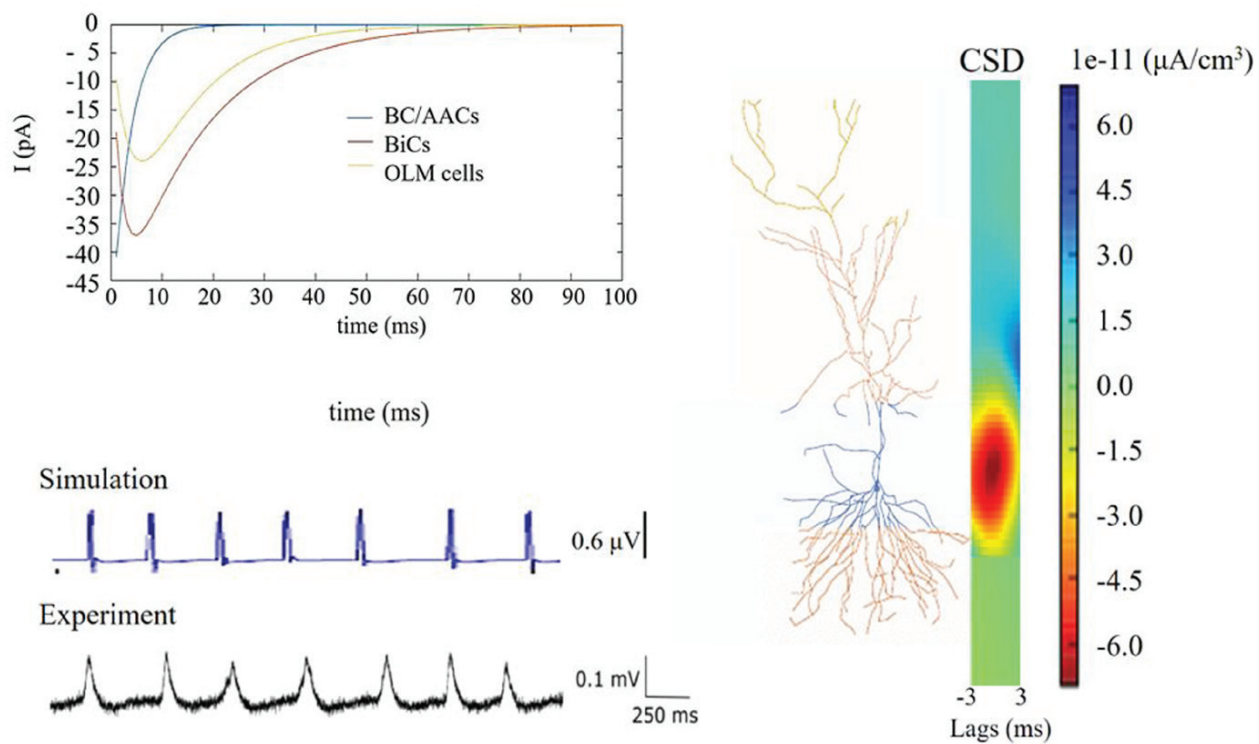
- 1014 **Maccaferri G**, David J, Roberts B, Szucs P, Cottingham CA, Somogyi P. Cell surface domain specific postsynaptic
 1015 currents evoked by identified GABAergic neurones in rat hippocampus in vitro. *The Journal of Physiology*.
 1016 2000 Apr; 524(1):91–116. <http://onlinelibrary.wiley.com/myaccess.library.utoronto.ca/doi/10.1111/j.1469-7793.2000.t01-3-00091.x/abstract>, doi: 10.1111/j.1469-7793.2000.t01-3-00091.x.
- 1018 **Makarova J**, Ibarz JM, Makarov VA, Benito N, Herreras O. Parallel Readout of Pathway-Specific Inputs to
 1019 Laminated Brain Structures. *Frontiers in Systems Neuroscience*. 2011; 5. <http://www.frontiersin.org/articles/10.3389/fnsys.2011.00077/full>, doi: 10.3389/fnsys.2011.00077.
- 1021 **Migliore M**, Migliore R. Know Your Current I_h: Interaction with a Shunting Current Explains the Puzzling Effects
 1022 of Its Pharmacological or Pathological Modulations. *PLOS ONE*. 2012 May; 7(5):e36867. <http://journals.plos.org/plosone/article?id=10.1371/journal.pone.0036867>, doi: 10.1371/journal.pone.0036867.
- 1024 **Ness TV**, Remme MWH, Einevoll GT. Active subthreshold dendritic conductances shape the local field potential.
 1025 *The Journal of Physiology*. 2016 Apr; p. 3809–3825. <http://onlinelibrary.wiley.com/myaccess.library.utoronto.ca/doi/10.1113/JP272022/abstract>, doi: 10.1113/JP272022.
- 1027 **Neymotin SA**, Lazarewicz MT, Sherif M, Contreras D, Finkel LH, Lytton WW. Ketamine Disrupts Theta Modulation
 1028 of Gamma in a Computer Model of Hippocampus. *The Journal of Neuroscience*. 2011; 31(32):11733–11743.
 1029 doi: 10.1523/JNEUROSCI.0501-11.2011.
- 1030 **Nicholson C**, Freeman JA. Theory of current source-density analysis and determination of conductivity tensor
 1031 for anuran cerebellum. *Journal of Neurophysiology*. 1975 Mar; 38(2):356–368. <http://www.physiology.org/doi/abs/10.1152/jn.1975.38.2.356>, doi: 10.1152/jn.1975.38.2.356.
- 1033 **Nunez PL**, Srinivasan R. *Electric Fields of the Brain: The Neurophysics of EEG*. Oxford University Press; 2006.
- 1034 **Petersen KH**, Lindén H, Dale AM, Einevoll GT. Extracellular spikes and CSD. In: Brette R, Destexhe A, editors.
 1035 *Handbook of Neural Activity Measurement* Cambridge University Press; 2012.p. 92–135.
- 1036 **Potworowski J**, Jakuczun W, Łęski S, Wójcik DK. Kernel Current Source Density Method. *Neural Computation*.
 1037 2012; 24:541 — 575.
- 1038 **Reimann MW**, Anastassiou CA, Perin R, Hill SL, Markram H, Koch C. A Biophysically Detailed Model of Neocortical
 1039 Local Field Potentials Predicts the Critical Role of Active Membrane Currents. *Neuron*. 2013 Jul; 79(2):375–390.
 1040 <http://www.sciencedirect.com/science/article/pii/S0896627313004431>, doi: 10.1016/j.neuron.2013.05.023.
- 1041 **Scheffer-Teixeira R**, Tort AB. On cross-frequency phase-phase coupling between theta and gamma oscillations
 1042 in the hippocampus. *eLife*. 2016 Dec; 5:e20515. <https://elifesciences.org/content/5/e20515v2>, doi:
 1043 10.7554/eLife.20515.
- 1044 **Schomburg EW**, Anastassiou CA, Buzsáki G, Koch C. The Spiking Component of Oscillatory Extracellular
 1045 Potentials in the Rat Hippocampus. *The Journal of Neuroscience*. 2012 Aug; 32(34):11798–11811. <http://www.jneurosci.org/content/32/34/11798>, doi: 10.1523/JNEUROSCI.0656-12.2012.
- 1047 **Siegle JH**, Wilson MA. Enhancement of encoding and retrieval functions through theta phase-specific manipula-
 1048 tion of hippocampus. *eLife*. 2014 Jul; 3:e03061. doi: 10.7554/eLife.03061.
- 1049 **Soltész I**, Losonczy A. CA1 pyramidal cell diversity enabling parallel information processing in the hippocam-
 1050 pus. *Nature neuroscience*. 2018 Apr; 21(4):484–493. <http://europemc.org/abstract/med/29593317>, doi:
 1051 10.1038/s41593-018-0118-0.
- 1052 **Spruston N**. Pyramidal neurons: dendritic structure and synaptic integration. *Nature Reviews Neuroscience*.
 1053 2008 Mar; 9(3):206–221. <http://www.nature.com/myaccess.library.utoronto.ca/nrn/journal/v9/n3/full/nrn2286.html>, doi: 10.1038/nrn2286.
- 1055 **Srinivas KV**, Buss EW, Sun Q, Santoro B, Takahashi H, Nicholson DA, et al. The Dendrites of CA2 and CA1
 1056 Pyramidal Neurons Differentially Regulate Information Flow in the Cortico-Hippocampal Circuit. *Journal of*
 1057 *Neuroscience*. 2017 Mar; 37(12):3276–3293. <http://www.jneurosci.org/myaccess.library.utoronto.ca/content/37/12/3276>, doi: 10.1523/JNEUROSCI.2219-16.2017.
- 1059 **Takács VT**, Klausberger T, Somogyi P, Freund TF, Gulyás AI. Extrinsic and local glutamatergic inputs of the rat
 1060 hippocampal CA1 area differentially innervate pyramidal cells and interneurons. *Hippocampus*. 2012 Jun;
 1061 22(6):1379–1391. <http://onlinelibrary.wiley.com/doi/10.1002/hipo.20974/abstract>, doi: 10.1002/hipo.20974.
- 1062 **Tendler A**, Wagner S. Different types of theta rhythmicity are induced by social and fearful stimuli in a network
 1063 associated with social memory. *eLife*. 2015 Feb; 4:e03614. doi: 10.7554/eLife.03614.

- 1064 **Wilson MA**, Varela C, Remondes M. Phase organization of network computations. *Current Opinion in Neuro-*
1065 *biology*. 2015 Apr; 31:250–253. <http://www.sciencedirect.com/science/article/pii/S0959438814002475>, doi:
1066 [10.1016/j.conb.2014.12.011](https://doi.org/10.1016/j.conb.2014.12.011).
- 1067 **Winson J**. Loss of hippocampal theta rhythm results in spatial memory deficit in the rat. *Science*. 1978 Jul;
1068 201(4351):160–163. <http://science.sciencemag.org/content/201/4351/160>, doi: [10.1126/science.663646](https://doi.org/10.1126/science.663646).
- 1069 **Łęski S**, Lindén H, Tetzlaff T, Pettersen KH, Einevoll GT. Frequency Dependence of Signal Power and Spatial
1070 Reach of the Local Field Potential. *PLoS Comput Biol*. 2013 Jul; 9(7):e1003137. [http://dx.doi.org/10.1371/](http://dx.doi.org/10.1371/journal.pcbi.1003137)
1071 [journal.pcbi.1003137](https://doi.org/10.1371/journal.pcbi.1003137), doi: [10.1371/journal.pcbi.1003137](https://doi.org/10.1371/journal.pcbi.1003137).

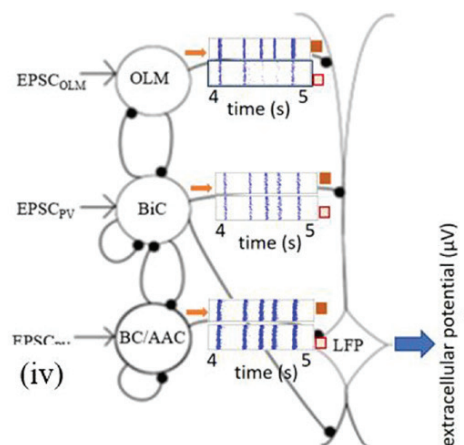
A.



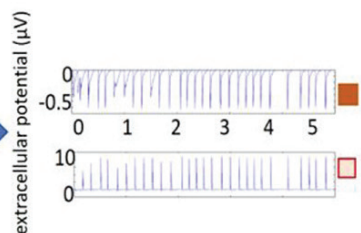
B.



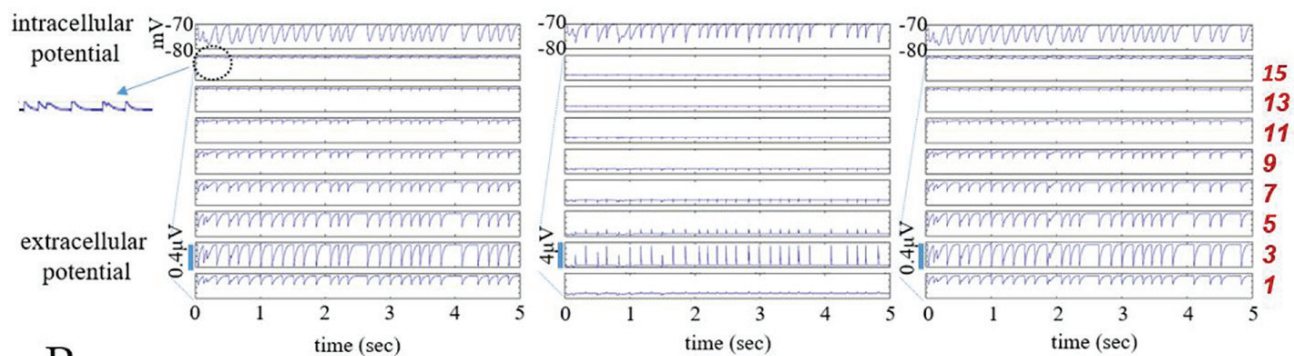
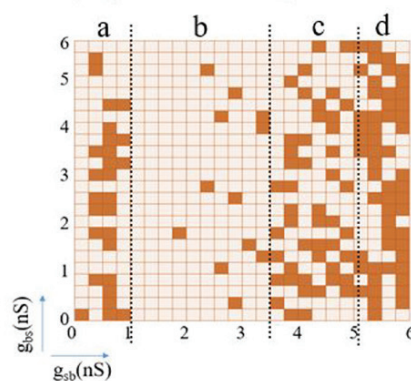
A. (i)



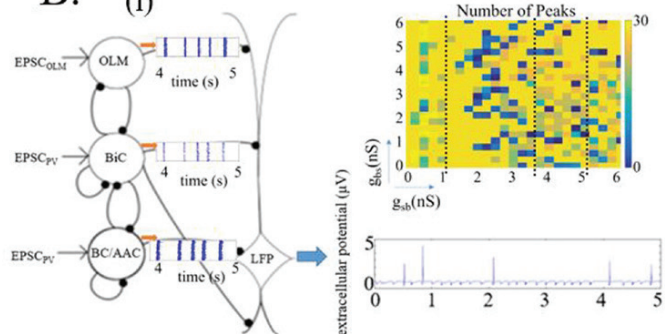
(ii)



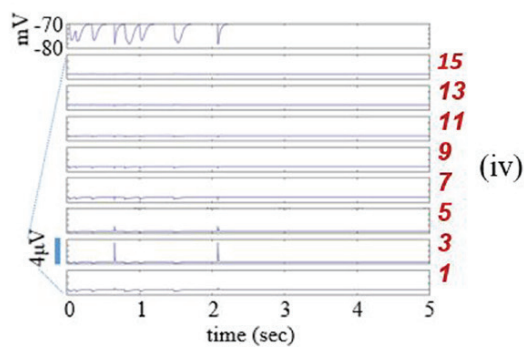
(iii) Polarity



B. (i)

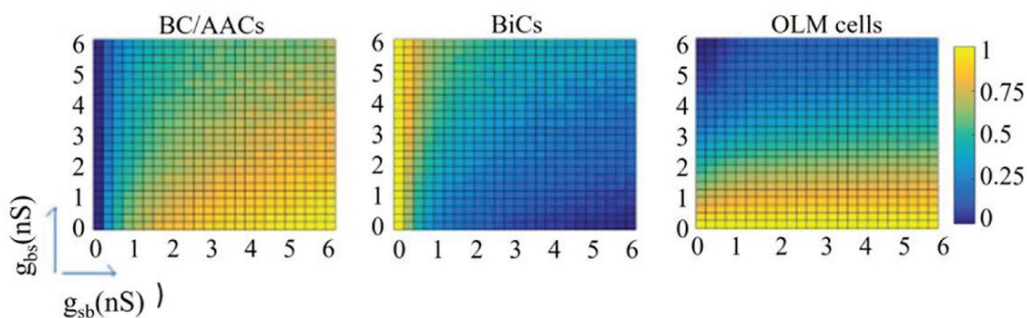


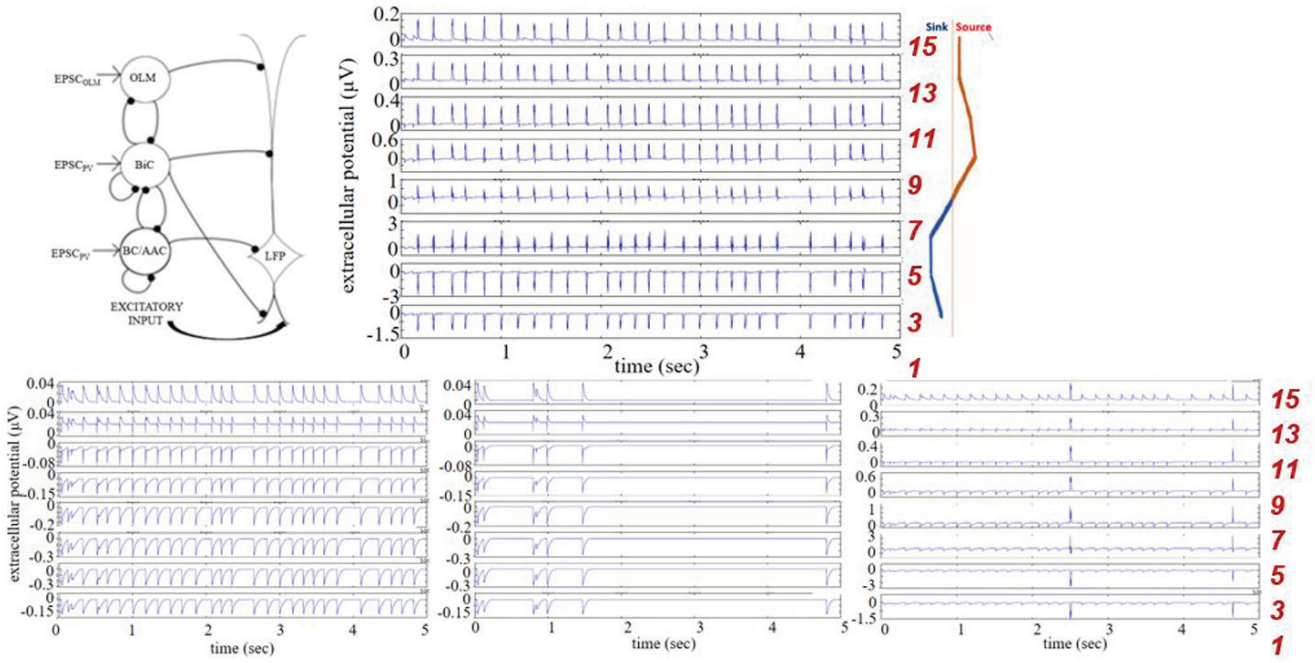
(iii)

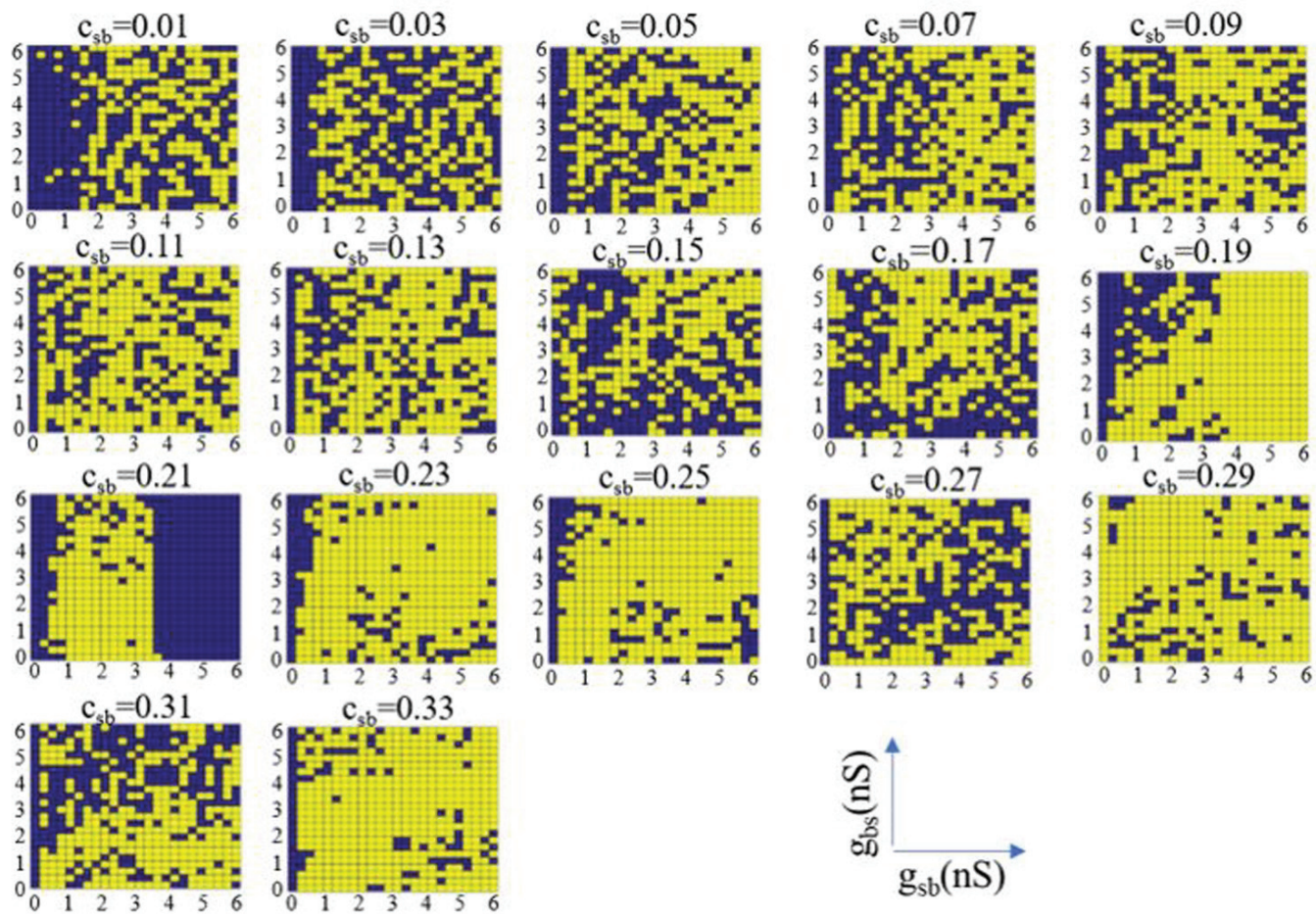


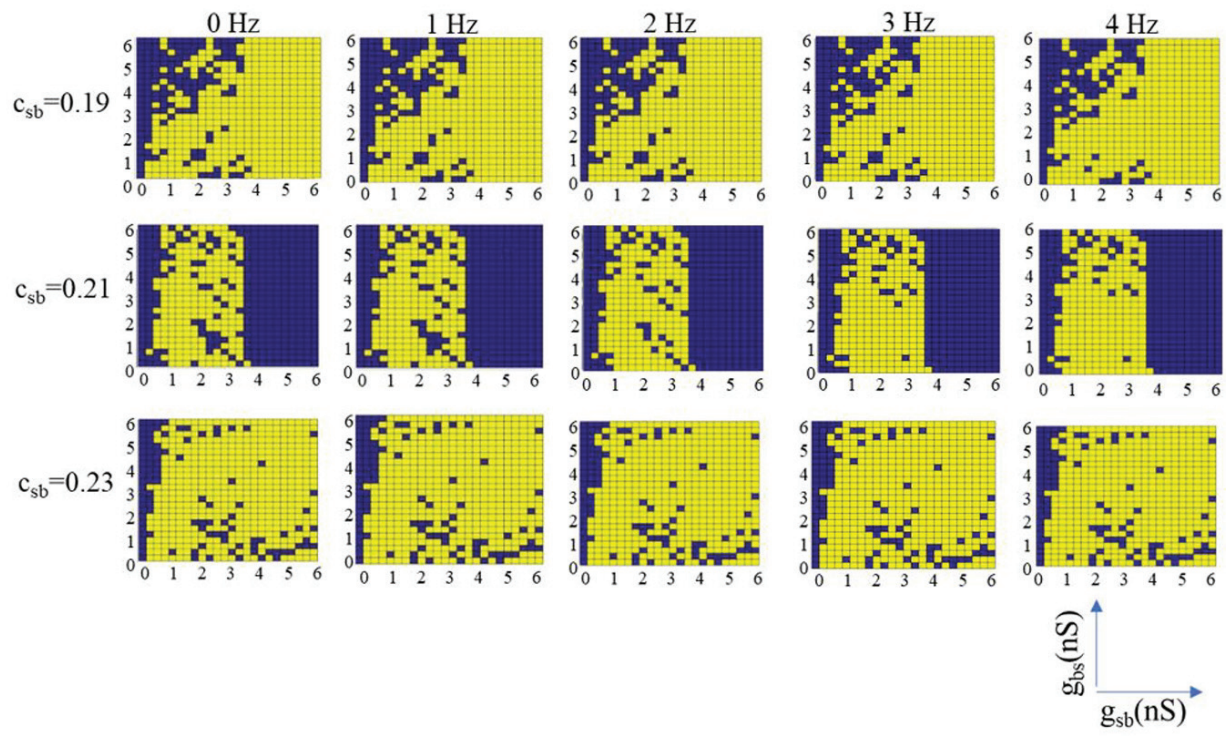
(ii)

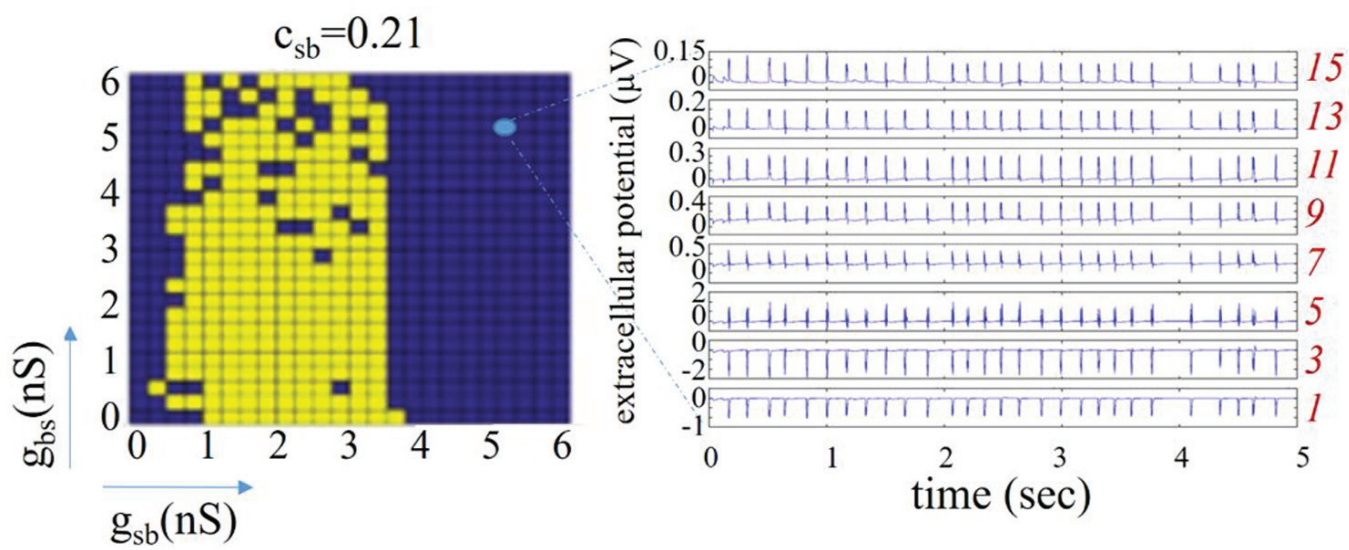
C.

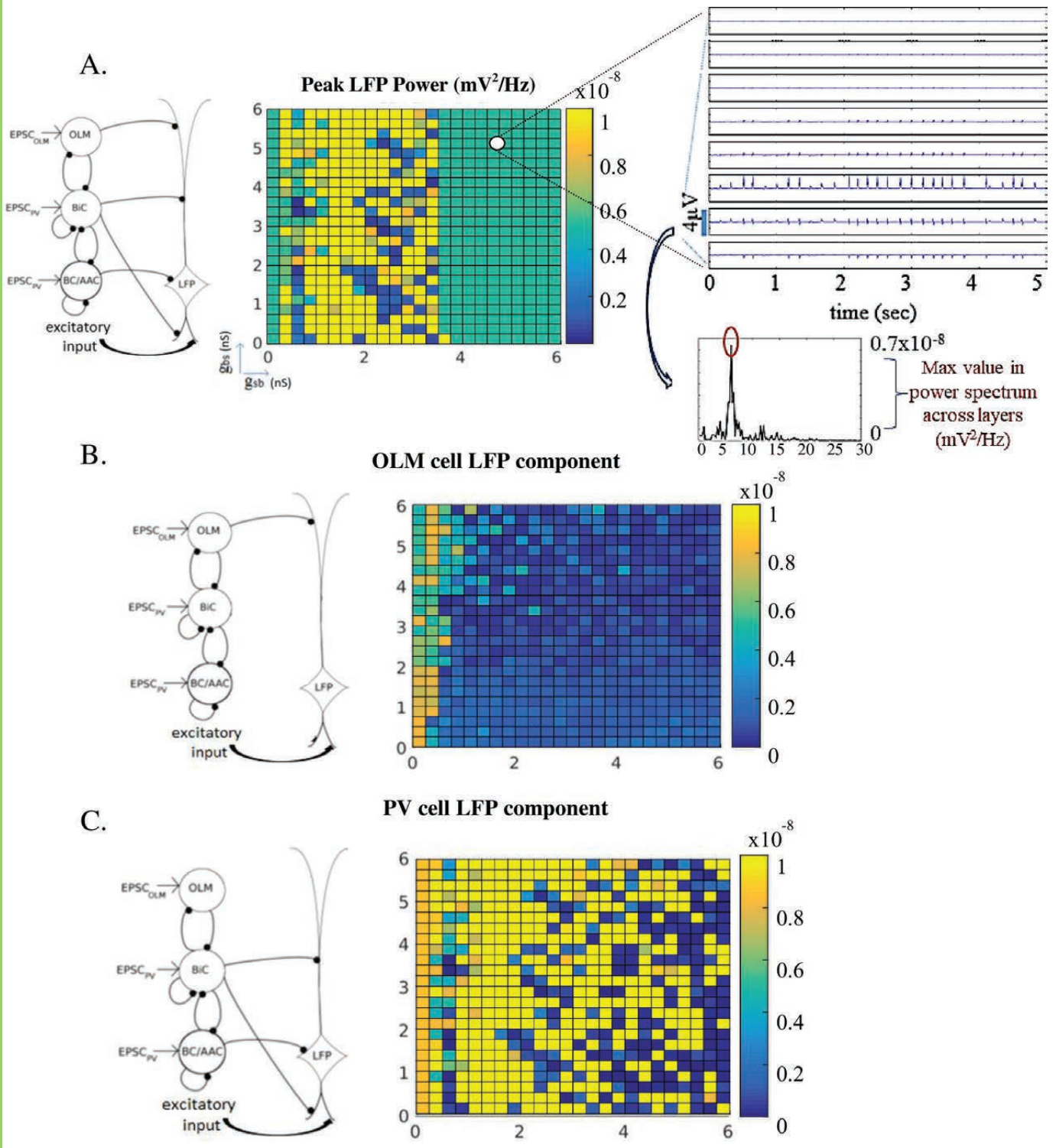


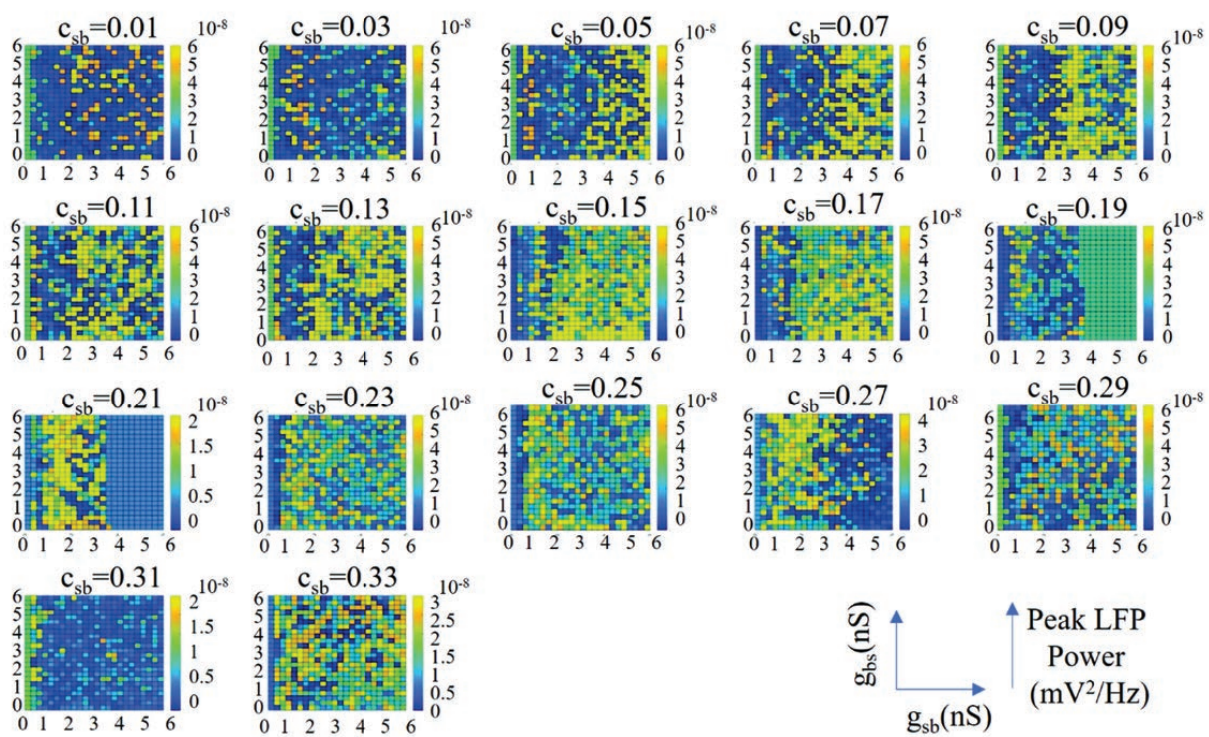


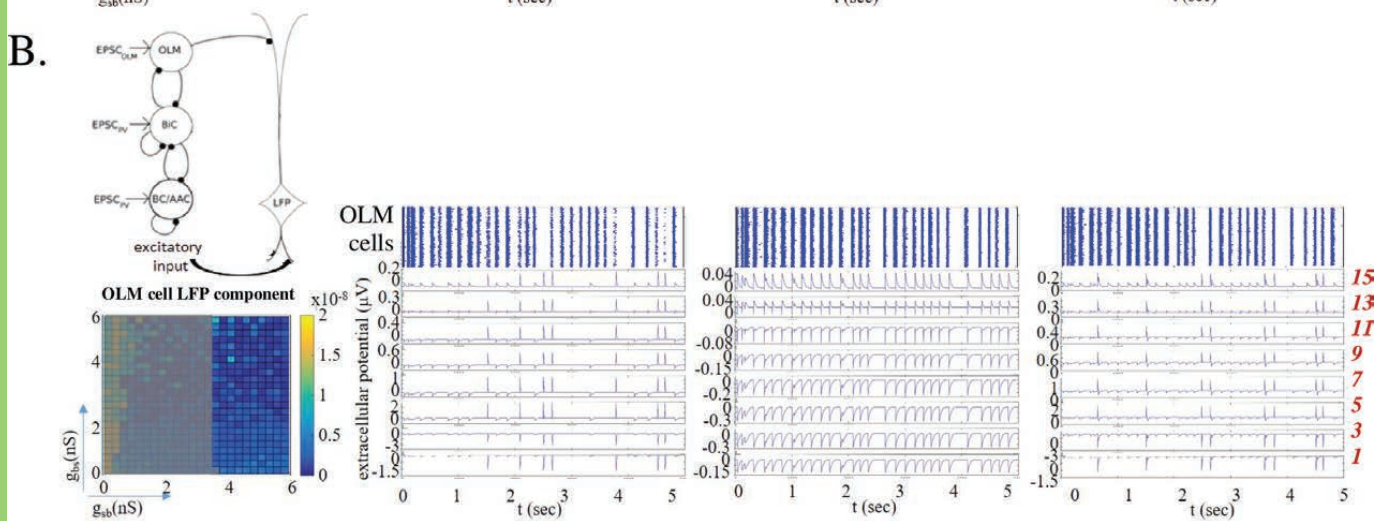
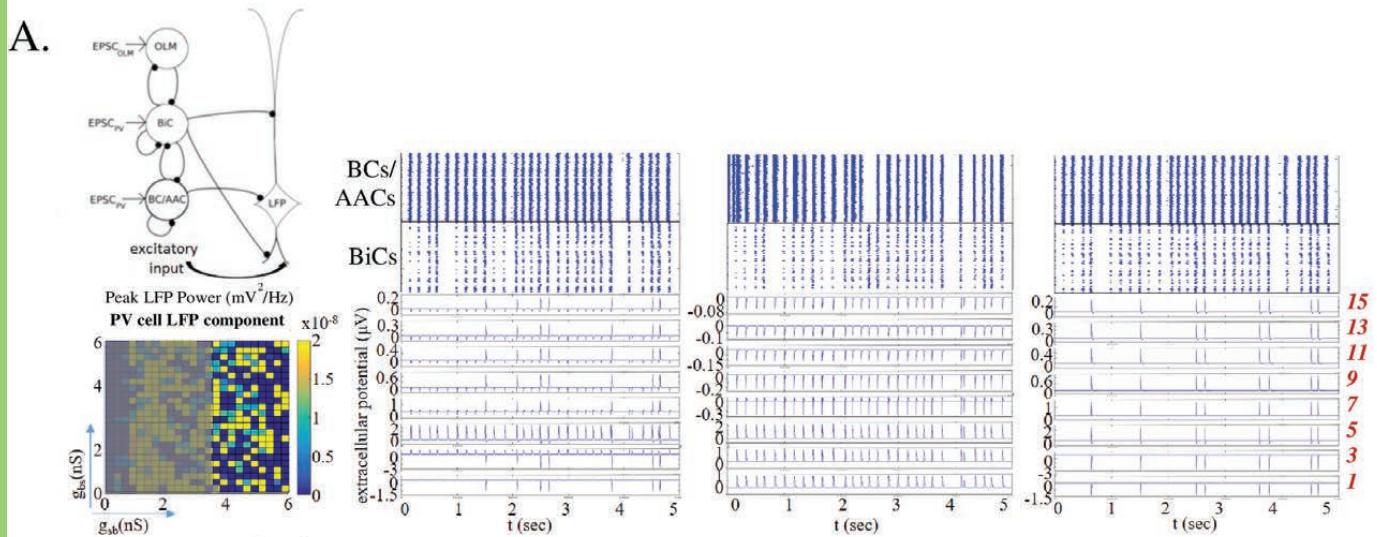








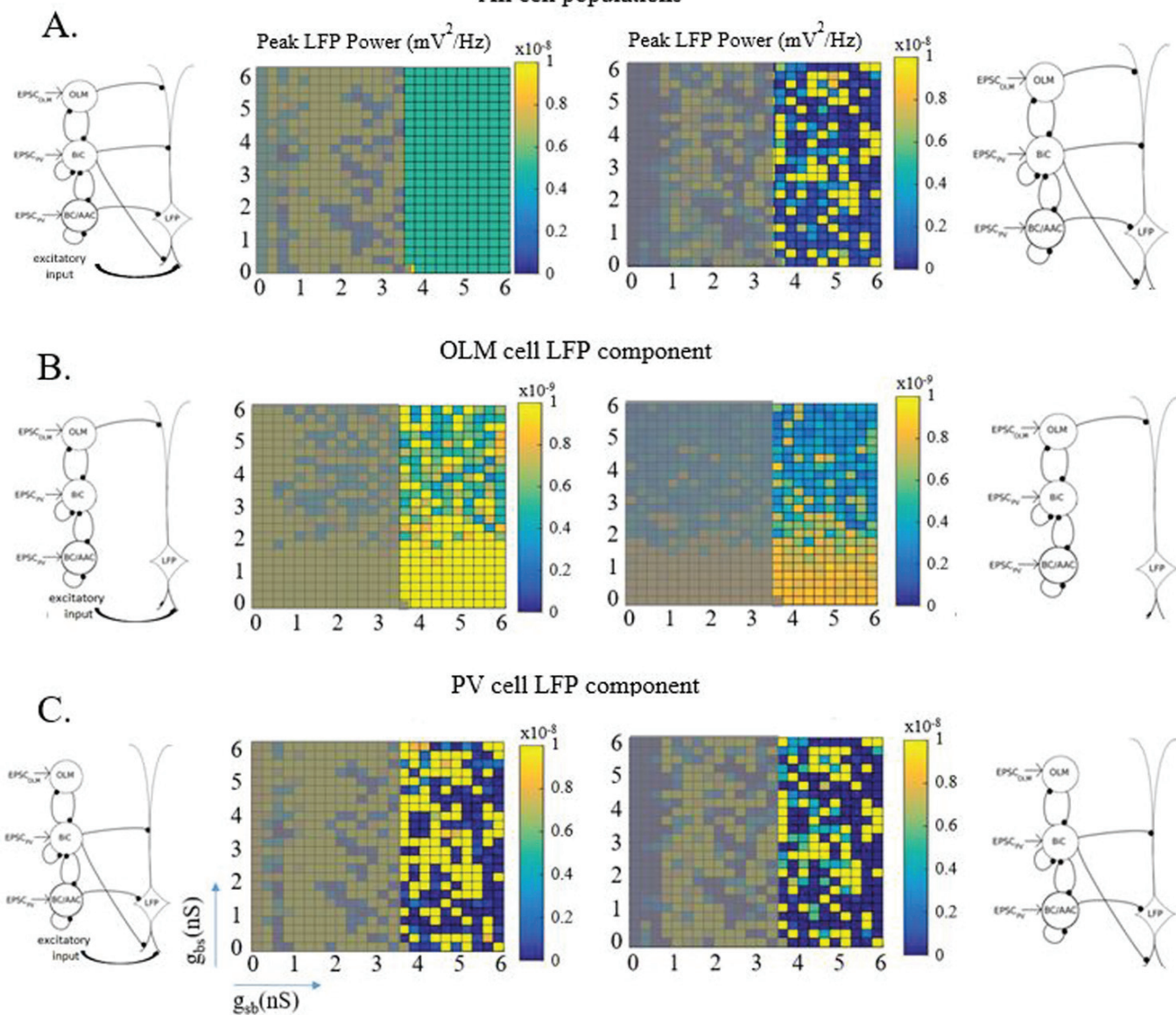




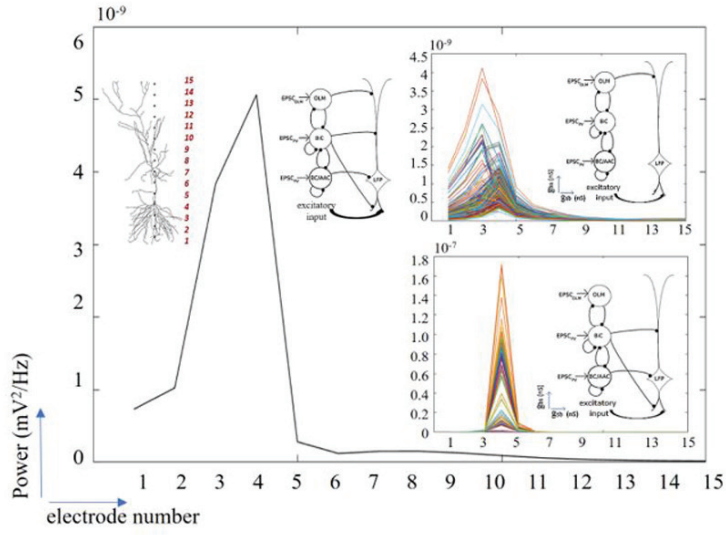
With basal excitation

Without basal excitation

All cell populations



A.



B.

